CSF1R-dependent macrophages control postnatal somatic growth and organ maturation.

Sahar Keshvari[#1], Melanie Caruso[#1], Lena Batoon[1], Anuj Sehgal[1], Ngari Teakle[1], Omkar L. Patkar[1], Cameron E. Snell[1], Chen Chen[2], Alex Stevenson[1], Felicity M. Davis[1], Stephen J. Bush[3], Clare Pridans[4], Kim M. Summers[1], Allison R. Pettit[1], Katharine M. Irvine*[1] & David A. Hume*[1]

1. Mater Research Institute-University of Queensland, Translational Research Institute, Woolloongabba, Brisbane, Qld 4102, Australia

2. School of Biomedical Sciences, University of Queensland, St Lucia, Qld, Australia

3. Nuffield Department of Clinical Medicine, John Radcliffe Hospital, University of Oxford, Oxford, UK,

4. Centre for Inflammation Research and Simons Initiative for the Developing Brain, Centre for Discovery Brain Sciences, University of Edinburgh, Edinburgh, UK

# These authors contributed equally.

* Joint senior authors

Address correspondence to David.Hume@uq.edu.au or Katharine.Irvine@uq.edu.au

Abstract

The development of the mononuclear phagocyte system (MPS) is controlled by signals from the CSF1 receptor (CSF1R). Homozygous mutation of the *Csf1r* locus (*Csf1rko*) in inbred rats led to the loss of non-classical monocytes and tissue macrophage populations, reduced postnatal somatic growth, severe developmental delay impacting all major organ systems and early mortality. The developmental impacts overlap with growth hormone/insulin-like growth factor (GH/IGF1) deficiency and *Csf1rko* rats lacked circulating IGF1. The liver is the main source of circulating IGF1. Expression profiling of juvenile wild-type and *Csf1rko* livers identified 2760 differentially expressed genes associated with the loss of macrophages, severe hypoplasia, delayed hepatocyte maturation, disrupted lipid metabolism and dysregulation of the GH/IGF1 system. Transfer of WT bone marrow at weaning restored circulating IGF1 and reversed the mutant phenotypes enabling long term survival and fertility. Phenotypic rescue was achieved without reconstituting blood monocytes or CSF1-responsive bone marrow progenitors. The results demonstrate that CSF1R-dependent macrophages control the growth and maturation of the liver and regulate the GH/IGF1 axis.

Running Title

The role of macrophages in postnatal development

Introduction

Resident macrophages are abundant in every tissue in the body and adapt to each tissue environment by expressing unique gene sets required for their local functions (reviewed in [1, 2]). Their differentiation from progenitor cells, their gene expression profile and their survival/maintenance in tissues is controlled by two ligands, colony stimulating factor 1 (CSF1) and interleukin 34 (IL34), which each signal through the CSF1 receptor (CSF1R) [3]. The biology of CSF1R and its ligands is conserved from birds to mammals [4-6]. In mice, the impacts of a homozygous *Csf1r* knockout mutation (*Csf1rko*) include perinatal mortality, postnatal growth retardation, increased bone density (osteopetrosis), global defects in brain development and abnormalities of the sensory nervous system, infertility and delayed pancreatic beta cell development (reviewed in [3, 7]). Many of the effects of the *Csf1rko* in mice are shared with mutations in the *Csf1* gene [3, 7].

Phenotypes associated with biallelic recessive mutations in human *CSF1R* are less severe. Patients present with abnormal skeletal development and calcification and selective loss of microglia in the brain leading to degenerative encephalopathy and brain malformations [8, 9]. We previously generated and characterised *Csf1rko* rats as an alternative model of human CSF1R deficiency [10]. To enable complementation of the *Csf1rko* mutation by transfer of bone marrow (BM) we have back-crossed the original outbred line to an inbred background. To explain the pleiotropic impacts in adults, in the present study we analyse the effect of the *Csf1rko* on tissue monocyte and macrophage populations and the growth and development of the skeleton and major organs in the early postnatal period. We show that CSF1R-dependent macrophages are essential in the liver for postnatal hyperplasia, hepatocyte functional maturation and lipid metabolism and that the pleiotropic *Csf1rko* phenotypes can be almost completely reversed by transfer of BM cells from WT congenic animals. Our findings demonstrate that expansion of resident tissue macrophage populations is a key event in

postnatal development that intersects with the growth hormone (GH)-insulin like growth factor (IGF1) axis to control somatic growth and organ development.

Results

The effect of *Csf1rko* on embryo survival and postnatal growth

The impact of the mutation on the inbred DA background remained clearly distinct from the pre-weaning lethality seen in inbred *Csf1rko* mice [3, 11, 12]. *Csf1rko* rats were indistinguishable from littermates at birth in either body size or morphology but by 3 wks they were less than 50% of the weight of wild-type (WT) controls. Most organs, including the liver, were proportionally reduced but the size of the brain was unaffected **(Figure S1A, B).** As reported previously, the relative growth advantage of males over females was also abolished **(Figure S1C)**. By 7 wks of age, the shape of the brain was clearly different between WT and *Csf1rko* rats, consistent with the radical difference in skull shape **(Figure S1D-F).** There was selective expansion of the lateral and third ventricles (**Figure S1E).** In the absence of expansion of the fourth ventricle (the major location of hydrocephalus in human patients) there was no gross impact on the size or conformation of the cerebellum, nor any histological difference in the Purkinje cell layers as shown by NeuN staining **(Figure S1F).** The one organ reduced disproportionately was the thymus, which was completely involuted in most animals by 7 wks.

The effect of the *Csf1rko* on skeletal development

The skeletal phenotype of the adult *Csf1rko* rat [10] closely resembles that of human CSF1R-deficient patients, referred to as dysosteosclerosis [8]. As shown in **Figure 1A,** the delay in skeletal development in the *Csf1rko* rats was already evident in newborns. By 3 wks of age secondary ossification centers of long bones and the small bones in the fore and hind paws were clearly deficient **(Figure 1B, C).** Unlike the hyper-calcified skull base [10], a shared feature with human bi-allelic *CSF1R* mutation [8, 9], the cranial case of the *Csf1rko* rats was hypomineralized even in adults and closure of the sutures was impaired **(Figure 1D).** The delay in musculoskeletal development was reflected in muscle. Sections through muscle at 7 days, 3 wks and 7 wks stained with laminin (**Figure**

1E,F) demonstrate that the relative cellularity was similar and the reduced muscle mass in the *Csf1rko* was primarily associated with a large reduction in muscle fibre diameter (i.e. failure of hypertrophy).

The effect of the *Csf1rko* on major organs

The *Csf1rko* led to developmental delay in all major organs. Because of the perinatal lethality in mice, the role of CSF1R-dependent macrophages in postnatal organ maturation has not previously been analysed. A subset of these organs is shown in **Figure S2.** In the rat, the process of nephrogenesis continues in the immediate postnatal period [13]. We therefore examined the development of the kidney in *Csf1rko* rats in detail. At 7 wks of age, we observed profound renal medullary hypoplasia, which was so severe that in most *Csf1rko* rats examined there was just a bud of papilla within the central pelvicalyceal space. The cortex was correspondingly hyperplastic, but the tubules and glomeruli appeared relatively normal **(Figure S2A, B).**

In the mouse digestive tract, CSF1-dependent macrophages control the stem cell niche at the base of the crypts and regulate the formation of antigen-sampling microfold (M) cells, Paneth cells and goblet cells [14]. The intestines of outbred adult *Csf1rko* rats were not grossly abnormal and by contrast to mice with the ligand mutation (*Csf1*$^{op/op}$), they were not Paneth cell deficient [10]. Quantitative analysis of villus architecture in the ileum **(Figure S2C-F)** showed significant reductions in the length and width of the crypts and villi, and the thickness of the submucosa in the *Csf1rko*. Macroscopic Peyer's patches were almost undetectable at 3 wks and remained so at later ages.

The main welfare concern with the *Csf1rko* is the development of progressive breathing difficulty. **Figure S2G** shows images of the inflated lungs of WT and *Csf1rko* rats at 3 wks stained with aldehyde-fuchsin to highlight elastin fibres and **Figure S2H** quantitates the airway space. There was no unequivocal evidence of impaired alveolisation. Flow cytometric analysis of disaggregated lung tissue revealed an increase in granulocytes in *Csf1rko* rats at 9 wks (**Figure S2I, J**), as seen in peripheral blood and BM, but there was no histological evidence of inflammation that could explain the impaired respiratory function.

The male and female inbred *Csf1rko* rats lacked development of primary and secondary reproductive organs[10]. In males, the prostate and seminal vesicles and in females the uterus were so under-developed as to be almost undetectable. CSF1R-dependent macrophages have also been implicated in the process of branching morphogenesis in the mammary gland in mice [15, 16]. **Figure S3** shows a comparison of mammary gland development in *Csf1rko* and WT female DA rats at around 9 wks. The negative impact of the mutation on ductal development was evident from staining with mature epithelial cell markers (Krt5, E-cadherin). The defective development is consistent with the reports in *Csf1*$^{op/op}$ mice [15, 16].

The effect of the *Csf1rko* on blood and bone marrow mononuclear phagocyte populations.

We next analysed the impacts of the *Csf1rko* on hematopoiesis. Both juvenile (3 wks) and adult (9 wks) *Csf1rko* rats exhibited an increase in circulating granulocytes **(Figure 2A, B).** Rat monocyte sub-populations are distinguished by reciprocal expression of the markers CD43 and HIS48, with HIS48^{Hi} and CD43^{Hi} monocytes corresponding to so-called classical and non-classical monocytes, respectively [17]. CD43^{Hi} non-classical monocytes are the large majority in rats [17]. In humans and mice the differentiation of non-classical monocytes (CD16^{Hi} and Ly6C^{Lo}, respectively) depends on CSF1 signalling [18, 19]. Consistent with the role of CSF1R signals in their differentiation, CD43^{Hi} monocytes were selectively lost in juvenile and adult *Csf1rko* rats but there was no corresponding increase in HIS48^{Hi} monocytes **(Figure 2C).** A significant reduction in circulating B cells was observed at 9 wks of age **(Figure 2D).**

Because of the osteopetrosis, BM cells could only be obtained from *Csf1rko* by crushing the femurs. There was a ~2-fold reduction in CD45^{+} leukocytes (as a proportion of live cells) recovered from *Csf1rko* BM and a relative increase in granulocytes **(Figure 2E, F).** After excluding granulocytes (HIS48^{Hi}/SSC^{Hi}), three monocyte/macrophage populations could be distinguished: two putative monocyte populations paralleling peripheral blood HIS48^{Hi} and CD43^{Hi} monocyte profiles, and a CD172A^{Low}/CD4^{+} BM resident macrophage population. Classical (HIS48^{Hi}) monocytes were more

abundant in WT BM than non-classical ($CD43^{Hi}$) monocytes, the reverse of peripheral blood. $CD172A^{Low}/CD4^{+}$ resident macrophages, as well as B cells, were selectively depleted in *Csf1rko* BM **(Figure 2G, H).**

The effect of the *Csf1rko* on tissue macrophages.

One explanation for the relative viability of *Csf1rko* rats compared to postnatal lethality in *Csf1rko* mice would be a differential dependence of tissue macrophages on CSF1R. To address the loss of tissue macrophages we stained for the abundant cytoplasmic calcium binding protein, IBA1, commonly used to identify microglia but shared with most other tissue macrophage populations in rats and mice [20-22]. As noted above, the *Csf1rko* rats were physically indistinguishable from littermates at birth. To determine whether there were any impacts on prenatal development we first examined the effect of the *Csf1rko* on macrophage populations in the embryo. IBA1 staining labelled the abundant macrophage populations in the liver and throughout the WT embryos at around 10.5 days of gestation whereas staining was almost absent in *Csf1rko* embryos in the same litters (**Figure 3A)**. A similar lack of $IBA1^{+}$ cells was observed at later gestational age (12.5-13.5dpc; not shown). One of the major functions of macrophages in the embryo is the clearance of apoptotic cells [23]. To examine this further we performed TUNEL (Terminal transferase-mediated dUTP-biotin nick end-labelling) staining to detect apoptotic cells. There was no evidence of accumulation of $TUNEL^{+}$ staining except for occasional cells in the liver **(Figure 3B).** One location where $CSF1R^{+}$ macrophages are actively involved in phagocytosis is the interdigital region [24]. However, we saw no evidence of delay in clearance of dying cells in this region despite the absence of $IBA1^{+}$ cells **(Figure 3A).**

Immunohistochemical localisation of IBA1 in selected organs from WT and *Csf1rko* rats at 3 and 7 wks is shown in **Figures 4 and 5.** In most WT tissues, IBA1 immunoreactivity was restricted to abundant interstitial stellate cells resembling macrophages. The extent and location of $IBA1^{+}$ populations was similar to our previous analysis of a rat *Csf1r*-mApple transgene [25] and much more

extensive than seen with anti-CD68 (ED1) [10]. *Csf1rko* led to substantial or complete loss of IBA1$^+$ cells in all organs examined except the lung. The WT kidney contained an abundant population of IBA1$^+$ interstitial cells similar in distribution to those identified previously in the mouse [26]. IBA1$^+$ cells were not detected in the kidneys of 3- and 7-week-old *Csf1rko* rats **(Figure 4A, F & 5A).** IBA1 staining also highlighted the abundant macrophage populations of the testis. In mouse testis, two distinct populations of macrophages have been described, interstitial and peritubular [27]. Both populations were absent in the *Csf1rko* rat testis at 3 wks and reduced at 7 wks. IBA1 is also expressed during sperm development, specifically in the cytoplasm of elongate spermatids and the residual bodies that are ultimately engulfed by Sertoli cells [20]. IBA1 staining indicated that the *Csf1rko* rat testis is not entirely deficient in sperm production **(Figure 4B & 5B)**. In the WT rat gut, IBA1 was detected on the abundant macrophage populations of the lamina propria, submucosa and muscularis of the small intestine, including those intimately associated with the crypts **(Figure 4C & 5C)**. The lamina propria populations were depleted in the *Csf1rko* (**Figure 4H**) associated with the narrowing of the villi (**Figure S2E),** but IBA1$^+$ cells were still detected associated with the base of the crypts. By contrast, IBA1$^+$ cells were absent from the submucosa and muscularis. Macroscopic Peyer's patches were difficult to find in the *Csf1rko*, but **Figure 4C & 5C** show sections through a small Peyer's patch from a *Csf1rko*, showing the retention of IBA1$^+$ cells underlying the follicle-associated epithelium (FAE). IBA1 is also expressed by the antigen-sampling M cells in the FAE [28] and these were also present and stained in the *Csf1rko*. Hence, unlike mice treated with anti-CSF1R antibody [14], the *Csf1rko* rats were not entirely depleted of M cells or lamina propria and crypt-associated macrophages.

The breathing difficulty we observe in *Csf1rko* rats with age was not reported in the *Csf1rko* mouse [29]. Respiratory failure also occurred in a severely-affected human infant with homozygous *CSF1R* mutation [9]. In the WT rat lung, IBA1 was detected in an abundant interstitial macrophage-like cell population and in cells within the airways that resembled alveolar macrophages (**Figures 4D & 5D)**.

Consistent with the known role of CSF2 (granulocyte-macarophage CSF) in lung macrophage homeostasis in mice and humans [30] the IBA1$^+$ population was not reduced in the *Csf1rko* rat lung at 3 wks of age (**Figure 4G**). In WT liver IBA1 staining highlights the extensive Kupffer cell population, and the density gradient of these cells from portal to centrilobular. There was a striking difference between the WT and *Csf1rko* livers at 3 and 7 wks. In the *Csf1rko* the number of IBA1$^+$ cells was reduced and they were concentrated around the portal vessels **(Figure 4E).**

In overview, IBA1 staining showed that the *Csf1rko* rats are grossly-deficient in tissue macrophages in most organs throughout embryonic and postnatal development.

The impact of *Csf1rko* on cell proliferation in liver, lung and kidney

The somatomedin hypothesis based initially on studies of hypophysectomized rats [31] proposed that postnatal somatic growth is controlled by pituitary growth hormone (GH) acting on the liver to promote release of insulin-like growth factor-1 (IGF1). The severe musculoskeletal growth phenotype of the rat *Csf1rko* resembles some impacts of mutations in the GH/IGF1 system [32]. The liver is a key target for GH and multiple hepatocyte-specific conditional mutations have confirmed hepatocytes as the major source of circulating IGF1 [33, 34]. CSF1 administration to adult mice, rats and pigs caused a rapid increase in the size of the liver associated with hepatocyte proliferation [17, 35, 36]. We reasoned that the *Csf1rko* might compromise postnatal liver growth and development leading directly or indirectly to the loss of serum IGF1. In rodents, liver mass increases several fold in the postnatal period reaching the adult liver/body weight ratio by around 4 wks of age [37, 38]. Consistent with that pattern, there was extensive proliferation of hepatocytes in WT rats at 3 wks detected by localization of Ki67. The proportion of Ki67$^+$ nuclei was reduced by >70% in the *Csf1rko* rats (**Figure 6A, D**). A reduction in cell proliferation was similarly observed in the *Csf1rko* kidney and lung. In the rat kidney, the medulla is relatively immature at birth and undergoes extensive proliferation and remodelling in the postnatal period [39]. As expected Ki67 labelling was mainly concentrated in the tubules and medullary rays in WT kidney at 3 wks. Consistent with the profound hypoplasia noted

above, in the *Csf1rko* kidney, Ki67^{+} staining was almost undetectable in the medullary epithelial cells **(Figure 6B, E).** The postnatal period in the rat is also a time of rapid lung development, associated with extensive cell proliferation [40], which was observed in WT and reduced in *Csf1rko* lungs (**Figure 6C, F)**.

The effect of the *Csf1rko* on gene expression in the liver.

Based upon the central role of the liver in GH-dependent control of somatic growth we next compared gene expression profiles of male and female *Csf1rko* and WT rats at 3 wks of age by RNA-seq to dissect the role of CSF1R-dependent macrophages in postnatal development and maturation of the liver. **Table S1A** contains the primary data and **Table S1B** shows 2760 differentially-expressed genes (DEG) distinguishing WT and *Csf1rko* livers (FDR <0.05). The DEG were grouped into a number of categories based upon known functions (i) growth factors (ii) Kupffer cell/macrophage-associated (iii) cell cycle-related; (iv) lipid metabolism (v) liver function/maturation-associated. **Figure 7A** summarises representative DEG in each category. Consistent with a possible impact of the mutation on circulating IGF1, the key genes significantly reduced in the *Csf1rko* included *Ghr, Igf1* and *Igfals* (which encodes a subunit of the major circulating IGF1 complex) whereas the inhibitory binding protein genes *Igfbp1*, *Igfbp2* and *Igfbp5* were amongst the most over-expressed transcripts in the 3 wk-old *Csf1rko* liver relative to WT. Aside from *Igf1*, known direct GH targets (e.g. *Socs2, Socs3, Cish;* [41]) were unaffected indicating that GH signalling was not impaired.

To identify gene co-expression networks we analysed the data using the analysis and visualisation tool BioLayout (http://biolayout.org). The sample-to-sample network graph for all transcripts revealed a clear separation based upon genotype but a lack of separation based upon sex (**Figure 7B)**. Clusters of co-expressed transcripts identified from a gene-to-gene correlation network are summarised in **Table S1C** and gene ontology (GO) terms for the largest clusters in **Table S1D. Figure 7C** shows the average profiles of the 4 co-regulated gene clusters that distinguished the WT and *Csf1rko*. The three clusters with lower average expression in the *Csf1rko* are consistent with the

relative loss of Kupffer cells (Cluster 6), reduced proliferation and cell cycle (Cluster 5) and delayed liver-specific differentiation (Cluster 2). Cluster 3, which contains transcripts expressed more highly, but variably, in the *Csf1rko* compared to WT is enriched for transcripts associated with mitochondria and oxidative phosphorylation.

Hepatic steatosis in the *Csf1rko* rat

Based upon the dysregulated expression of genes involved in lipid metabolism in the *Csf1rko* rats we investigated whether this might lead to lipid accumulation, which could be related to or compounded by the complete lack of visceral adipose tissue [10] also evident in the inbred line. As observed previously [42] the livers of both WT and *Csf1rko* rats were mildly steatotic at 3 wks of age. Whereas this resolved with age in WT there was progressive and extensive steatosis in the liver of older *Csf1rko* rats (**Figure 8A).** Because of the failure of tooth eruption, *Csf1rko* rats were maintained on a modified diet. However, steatosis was not observed in the livers of WT rats maintained for 12 wks with access to the same diet. The *Csf1*$^{op/op}$ mouse has been reported to have a substantial deficit in insulin-producing cells in the pancreatic islets [43]. The selective loss of adipose tissue might suggest the reverse in the *Csf1rko* rat. We therefore measured circulating fed glucose and insulin levels and found minimal differences between WT and *Csf1rko* at 7 wks of age (**Figure 8B, C).**

Rescue of the *Csf1rko* phenotype by wild type bone marrow cells.

To determine whether the developmental abnormalities in the *Csf1rko* were autonomous to hematopoietic lineage cells and reversible, we treated a cohort of 3 wk-old *Csf1rko* rats with WT congenic BM cells by IP injection without conditioning. By 2-3 wks post BM transfer the body weight gain of recipients diverged from *Csf1rko* controls and continued to increase thereafter **(Figure 9A).** Based upon the reduced liver growth and altered gene expression we measured circulating IGF1 and GH. In WT rats, there was a post weaning surge in IGF1 followed by a gradual decline **(Figure 9B)** whereas IGF1 was barely detectable in the serum of *Csf1rko* rats at any age. By contrast, consistent with the expression of GH target genes in the liver (see above), the circulating

concentration of GH was unaffected **(Figure 9C)**. In the *Csf1rko* rats that received WT BM, IGF1 was increased by 4 wks post transfer (week 7) and peaked at 6 wks **(Figure 9B).** The transfer of WT BM cells populated the liver with macrophages of donor origin, as shown by the expression of *Csf1r* and *Adgre1* mRNA **(Figure 9D, E).** The appearance of the animals changed rapidly, notably the skull and limb/foot morphology, so that by 6 wks post-transplant they resembled WT animals **(Figure 9F-H).** The steatosis observed in untreated *Csf1rko* rats remained 4 wks post BM transfer but resolved by 9 wks **(Figure 9I).** Both males and females became sexually mature and fertile and produced multiple litters. The females were able to suckle their offspring indicating restoration of mammary function. At necropsy up to 6 months post BM transfer, the body weights were around 10% lower than littermates (**Figure 9A**) but visceral adipose was restored in both sexes and major organ histology was indistinguishable from controls. The ventricular enlargement in the brain was still detected but had not progressed beyond the extent observed at 3 weeks.

Nine wks post BM transfer, peritoneal macrophages were restored to the level of WT controls with indistinguishable surface marker profiles **(Figure 10A-C)**. Surprisingly, the BM transfer did not restore the $CD43^{Hi}$ blood monocyte population in the rescued *Csf1rko* rats whilst the granulocytosis and B cell deficiency in peripheral blood was resolved **(Figure 10D-F).** The BM cavity was patent and the yield of $CD45^{+}$ leukocytes obtained by flushing was similar to WT. The $CD172^{Lo}/CD4^{+}/HIS48^{-}/CD43^{Lo}$ resident macrophage population was partially restored and granulocyte and B cell numbers were normalised following BM transfer **(Figure 10G-I)** but the harvested BM cells did not respond to CSF1. In standard liquid cultures used routinely to generate BM-derived macrophages in our laboratory [44] BM cultured from rescued *Csf1rko* had few or no surviving cells after 7 days in culture whereas WT controls produced a confluent macrophage culture **(Figure 10J).** These findings indicated that the BM progenitor cell compartment remains of recipient *Csf1rko* origin.

Discussion

The role of CSF1 in postnatal growth

The relative abundance of macrophages increases in every organ of the mouse in the first 7-14 days of life, associated with a 3-5 fold increase in *Csf1* mRNA in whole body and in individual organs [45]. Our results demonstrate that CSF1R-dependent macrophages are essential for normal postnatal development in the rat and that they act in part via regulation of the GH/IGF1 axis. As noted above, the somatomedin hypothesis proposed that somatic growth is controlled by pituitary GH acting on the liver to control the production of IGF1. Numerous analyses of conditional mutations of *Ghr, Igf1* and *Igf1r* in various tissues and cell types in mice paint a more complex picture [33, 34, 41]. Conditional deletion of *Igf1* in the liver had a marginal effect on somatic growth despite 70-90% loss of circulating IGF1 [33, 34]. The loss of circulating IGF1 in *Csf1rko* rats, which was rescued by transfer of WT BM cells, indicates that CSF1R-dependent macrophages control circulating IGF1 levels. Macrophages themselves produce an array of growth factors, including IGF1, that are implicated in development and tissue repair [7, 46]. Meta-analysis of mouse resident tissue macrophage gene expression [47] revealed constitutive high expression of *Igf1* and *Igfbp4* mRNA but macrophages are clearly not the only extrahepatic source. Conditional deletion of *Igf1* in myeloid cells in mice had no reported effect on somatic growth although it did imply a role for macrophage-derived IGF1 in visceral adipose [48]. Accordingly, we suggest that CSF1R-dependent macrophages act indirectly through their effects on hepatocyte proliferation and maturation.

The effect of the *Csf1rko* on the liver.

The set of hepatic genes correlated with *Csf1r* in network analysis **(Figure 7A, Table S1C)** includes *Cd68* and *Aif1,* encoding proteins (CD68 and IBA1 respectively) and provides a Kupffer cell (KC) signature that marker genes enriched in this resident population in mice (e.g. *Cd5l, Clec4f, Timd4, Vsig4*) [49, 50]. The liver has a unique ability to regenerate following partial hepatectomy to return to a constant liver-body weight ratio, a so-called hepatostat [51]. Administration of CSF1 to adult

mice, rats or pigs [25, 35, 36, 52] overcomes this constraint, drives hepatocyte proliferation and accelerates regeneration following partial hepatectomy. During the postnatal period in rat liver a phase of hyperplasia is followed by hypertrophy and structural maturation to form mature hepatic sinusoids lined by a single layer of hepatocytes [37]. Treatment of neonatal rats with CSF1 in the first 5 days of life produced >30% increase in liver weight and expansion of the Kupffer cell population [42]. The substantial reduction in hepatocyte proliferation in the juvenile *Csf1rko* rat confirms the causal link. We propose that severe inhibition of hepatocyte proliferation *per se* is sufficient explanation for the loss of circulating IGF1 to support somatic growth in the *Csf1rko.* In keeping with this view, a hepatocyte-specific deletion of *Jun* in mice that reduced postnatal hepatocyte proliferation also impaired somatic growth [53]. The impact of reduced hepatocyte proliferation in *Csf1rko* is compounded by the reduced relative expression of *Ghr, Igf1, Igfals* and over-expression of the inhibitory *Igfbp* family members demonstrated in RNA-seq analysis. The impact of alterations in the liver on production of circulating IGF1 is likely compounded by impacts of the *Csf1rko* on local IGF1 production in other tissues, leading indirectly to increased tissue consumption of the circulating protein.

In addition to impacts of the *Csf1rko* on the IGF1 axis in the liver, transcriptional profiling indicated a broader delay in postnatal hepatocyte maturation exemplified by the retention of fetal liver-expressed genes such as lipoprotein lipase (*Lpl*)[54], fetal liver hepcidin (*Hamp*) [55] and the fetal amino acid transporter *Slc38a2* [56]. Two other genes highly enriched in the liver of *Csf1rko* rats were the cold shock-inducible gene *Rbm3* and stress-inducible *Gadd45b*. Expression of *Rbm3* and *Gadd45b* and their potential impacts on liver metabolism [57, 58] could be a consequence and/or a cause of the reduced adiposity and hepatic steatosis of the *Csf1rko.* Conversely, the relative loss of several highly expressed liver-specific genes is likely to exert additional pleiotropic effects on other organs. For example, SERPINA6 (transcortin) is the major binding protein for circulating glucocorticoids implicated in regulation of the response to GH [59].

The liver of 7-day old rats contains abundant lipid droplets [42] but this usually resolves rapidly. The coordinated reduction of numerous genes involved in lipid metabolism **(Figure 7A)** in the liver in 3 wks *Csf1rko* is the reciprocal of the increase observed following CSF1 treatment of neonates [42] and may contribute to both the progressive steatosis and the lack of visceral adipose in the animals. Both of these phenotypes were reversed by the transfer of wild type BM cells **(Figure 9).** The coordinated regulation of genes involved in lipid metabolism may be related to the reduced expression of the transcriptional repressor *Hes6* [60] in the *Csf1rko.* The expression data reveals one possible contribution to the loss of macrophages in control of hepatocyte proliferation. The activin/follistatin axis controls of liver growth [61] and genes encoding three of the activin subunits (*Inhba, Inhbc, Inhbe*) were reduced in the *Csf1rko* livers whereas the inhibitory follistatin (*Fst*) was increased.

The effect of Csf1rko on skeletal development.

Although there are similarities in some phenotypes, the osteosclerotic bone phenotype in the *Csf1rko* is quite distinct from osteopenia associated with GH or IGF1 deficiency [32]. The phenotype relates to the process of intramembranous ossification. Intramembranous bones ossify directly from preosteogenic condensations of multipotent mesenchymal stem cells without a chondrocyte intermediate. Like endochondral ossification, this process is dependent upon angiogenesis (reviewed in [62]). The process of bone formation in the cranial case is initiated by postnatal expansion of bone from the sutures formed during embryonic development [63]. Osteoblast maintenance and calcification requires input from osteomacs, a bone-associated macrophage population distinct from osteoclasts [64]. These CSF1-responsive macrophages promote the processes of both endochondral and intramembranous ossification during bone repair *in vivo* [65, 66]. Accordingly, we propose that the selective failure of intramembranous ossification in the cranial case, and the increased calcification of the base of the skull, reflect distinct functions of osteomacs and osteoclasts, both dependent on CSF1R.

The *Csf1rko* rat resembles bi-allelic human *CSF1R* mutation in the pronounced under-modelling of the digits [8]. Detailed analysis of digital development in the mouse [67] revealed morphologic and calcification patterns in the subarticular regions that were also distinct from archetypical physeal endochondral ossification. The defects we observe in the *Csf1rko* rats resemble skeletal dysplasia caused by mutations in the gene encoding the macrophage-enriched transcription factor MAFB [67] and more generally various forms of malignant osteopetrosis (reviewed in [68]).

The role of Csf1r-dependent macrophages in development of other organ systems.

As previously observed on an outbred background [10] inbred *Csf1rko* rats had few detectable blood monocytes. Here we showed that this loss of monocytes is selective for the CD43^{Hi} 'non-classical' monocyte population which is the major population in the rat [25]. Analysis of a hypomorphic *Csf1r* mutation [69] and the selective impact of anti-CSF1R antibody [18] indicates that CSF1R is not required for monocyte production, whereas tissue macrophages require CSF1 for survival. In many different organ systems, depletion of resident tissue macrophages permits monocyte extravasation to occupy the vacant territory or niche (reviewed in [1, 2]). The lack of accumulation of classical (His48^{Hi}) monocytes in the *Csf1rko* despite the block to maturation could reflect more rapid transit in the circulation. For example, the striking periportal concentration of the residual IBA1^{+} Kupffer cells in the liver **(Figure 4D & 5D)** and reduced numbers in the gut lamina propria **(Figure 4H)** could be associated with continuous extravasation of monocytes and subsequent short half-life in the tissue.

Analysis of the role of macrophages in postnatal development based upon *Csf1r* and *Csf1* mutations in mice has focussed on one organ at a time, emphasising local functions [3]. In view of the impacts of the *Csf1rko* on the liver and circulating IGF1 we cannot separate direct local roles of macrophages in the regulation of proliferation and differentiation in organs such as brain, lung, kidney, gut, adipose and gonads from systemic consequences of liver dysfunction.

Given the large numbers of macrophages in the developing embryo and their roles in clearance of apoptotic cells [23] it is surprising that there is so little apparent impact of their almost complete

absence in the *Csf1rko* on prenatal development. We suggest that other cells can fulfil the phagocytic functions of macrophages in embryonic development. In keeping with this view, although genes encoding lysosomal enzymes and endosome-associated proteins are highly-expressed by microglia, the relative expression of these genes was unaffected in brains of *Csf1rko* rats or microglia-deficient mice [10, 69].

The nature of the progenitor cells that mediate phenotypic rescue

Pre-weaning lethality was prevented in around 50% of *Csf1rko* mice by neonatal transfer of WT BM cells [11]. In the rat, we were actually able to reverse and rescue the *Csf1rko* phenotype by transfer at weaning with 100% success. The recipients were not treated to deplete hematopoietic stem cells (HSC) and were not deficient in other blood cell lineages. The reversal of osteosclerosis and restoration of the BM hematopoietic niche likely requires the generation of CSF1R-dependent osteoclasts and resident osteomacs and hematopoietic island macrophages [70, 71]. Further studies will be required to confirm that osteoclasts and the resident macrophages detected in the rescued marrow are of donor origin. However, the implication of the lack of CSF1 responsiveness in BM in the rescued *Csf1rko* rats is that there is a committed progenitor in rat BM that can directly provide long term engraftment of tissue mononuclear phagocyte populations. The key donor population is likely related to the CSF1-responsive clonogenic monocyte progenitor described in mouse BM [72]. Studies in the chick also revealed the existence of a BM progenitor that could produce long term macrophage--restricted chimerism when injected into the embryo prior to the onset of definitive hematopoiesis [4]. Further characterization of macrophage progenitor populations in the rat will depend on development of surface markers that are not currently available.

The second key implication of the rescue of the *Csf1rko* relates to the origins of resident macrophages. There is an emerging view based upon lineage trace models in mice that most tissue macrophages are seeded during embryonic development and thereafter maintained by self-renewal [1, 2]. Whether or not this model can be extended to other species, the long-lived effectiveness of the rescue of *Csf1rko*

rats indicates that macrophages macrophage territories in every organ can be occupied by cells of BM origin and maintained in the absence of CSF1R-expressing monocytes.

Conclusion

The developmental impact of the *Csf1rko* in the rat is clearly distinct from the mouse, even when compared to the original outbred mouse *Csf1rko* line where there was less perinatal lethality and evidence of age-dependent recovery [29]. The analysis of IBA1^{+} tissue macrophage populations (**Figures 4 and 5**) indicates that if anything the *Csf1rko* has a greater impact in rats than the partial and selective loss of macrophages observed in outbred mice [29]. Several studies in mice have claimed that the *Csf1r* gene is expressed outside the MPS and some phenotypic impacts of the mouse *Csf1rko* have been attributed to expression in neurons, intestinal and renal epithelia and the reproductive tract [3]. These claims were not supported by critical analysis which instead favoured the exclusive expression of *Csf1r* in MPS cells (Reviewed in [6]). We recently provided direct evidence for the MPS lineage restriction of CSF1R expression in mice on the basis of a knock-in reporter transgene [73]. The advantage of the rat *Csf1rko* model is the increased postnatal viability even on an inbred background, enabling us to demonstrate that the quite severe developmental phenotype of the *Csf1rko* can be almost entirely reversed. Taken together, the mouse and rat data further confirm that functional expression of *Csf1r* is restricted to BM-derived cells. The reversal of the phenotypic impacts of the *Csf1rko* will enable analysis and optimization of therapeutic options for patients with CSF1R deficiency [74]. More broadly, many of the impacts on organ development and consequent morbidity in the *Csf1rko* rat are shared with premature human infants. The rat transplant model provides a unique system in which to define the pathways of development of resident tissue macrophages and their local and systemic roles in growth and organ maturation.

Material and Methods

Generation of transgenic rats and animal maintenance.

To create a pure DA line the original outbred *Csf1rko* was backcrossed to WT DA (Animal Resource Centre, Perth, Australia) for at least 7 generations. As *Csf1rko* rats do not develop teeth, to ensure their survival and maximise their growth we routinely separate them from their littermates at 3 wks and commence a feeding regime including wet mashed standard chow and a veterinary powdered milk nutritional supplement (Di-Vetelact, Sydney, Australia). The same approach is used in maintenance of *Csf1*$^{op/op}$ mice (e.g. [43]). Rats were bred and maintained in specific pathogen free facilities at The University of Queensland (UQ) under protocols approved by the UQ Animal Ethics Unit.

Bone marrow transfer

Bone marrow was obtained from the femurs and tibias of WT rats by flushing with a 26G needle. $1x10^7$ bone marrow cells in saline solution containing 2% fetal bovine Serum (FBS) were transferred to 3 wk-old *Csf1rko* recipients by intraperitoneal injection. Recipients were maintained on the supplemented diet.

Flow cytometry

100 ul peripheral blood was collected into ethylenediaminetetraacetic acid (EDTA) tubes by cardiac puncture after CO_2 euthanasia. Red cells were lysed for 2 min in ACK lysis buffer (150mM NH_4Cl, 10mM $KHCO_3$, 0.1mM EDTA, pH7.4), the leukocytes were centrifuged and washed twice in PBS and the pellet resuspended in flow cytometry (FC) buffer (PBS/2%FBS) for staining. Cells were stained for 45 min on ice in FC buffer containing unlabelled CD32 (BD Biosciences, Sydney, Australia) to block Fc receptor binding and HIS48-FitC, CD11B/C-BV510, CD45R-PE (BD Biosciences), CD43-AF647, CD4-APC/Cy7 (Biolegend, San Diego, CA, USA) and CD172A-AF405 (Novus, Noble Park North, Australia). Cells were washed twice and resuspended in FC buffer containing 7AAD (LifeTechnologies, Musgrave, Australia) for acquisition on a Cytoflex flow

cytometer (Beckman Coulter Life Sciences, Sydney, Australia). Single colour controls were used for compensation and fluorescence-minus-one controls were used to confirm gating. Data were analysed using FlowJo 10 (Tree Star; https://www.flowjo.com).

Micro-CT imaging and reconstruction

Bones for micro-CT were fixed in 4% paraformaldehyde (PFA) and scanned using Bruker's Skyscan 1272 (Bruker, Belgium) by rotating over 360° in 0.8° rotational steps. The X-ray settings were standardised to 70 kV and 142 µA with an exposure time of 1450 ms and the X-ray filter used was a 0.5 mm aluminium. Projections were acquired with nominal resolutions of 21.5 and each resulting image contained 1144 x 1144 pixels. All X-ray projections were reconstructed using NRecon 1.7.3.1 software (Bruker) to create cross-sectional images and viewed using CTvox 3.3.0 (Bruker).

Bone immunohistochemistry (IHC) and histological staining

Fixed bones were decalcified in 14% EDTA for 8-10 wks. IHC was performed on deparaffinized and rehydrated 5 µm sections with biotinylated anti-laminin antibody (Novus Biologicals, Colorado, USA). Sections were blocked for endogenous peroxidase activity using 3% hydrogen peroxide and antigens were retrieved using 0.5% Pepsin (Sigma-Aldrich, Sydney, Australia). Non-specific staining was blocked using 10% FBS/neonatal goat serum (NGS) prior to 90 min incubation with anti-laminin antibody followed by HRP-conjugated streptavidin for 30 min. Diaminobenzidine was developed as per the manufacturer (Vector Labs, California, USA) instructions and all sections were counterstained with Mayer's hematoxylin (Sigma-Aldrich). Whole-mount Alcian Blue-Alizarin Red staining of newborn rats was performed as previously described [75]. Staining was imaged using VS120 slide scanner (Olympus, Tokyo, Japan) or SZX10 stereo microscope with DP26 digital camera (Olympus). Laminin-stained sections from 3-week-old rat limbs were used to examine the muscle fiber diameter of the posterior tibialis. The average diameter of 30 muscle fibers was analyzed using Visiopharm® software (Visiopharm, Hørsholm, Denmark).

Brain immunohistochemistry

Rat Brains were harvested and fixed in 4% paraformaldehyde for 48 h and then transferred into PBS containing 0.01% azide. Brains were sectioned in the sagittal plane using a vibratome (Leica VT 1200S, Leica Biosystems, Mt Waverley, Australia). Free-floating sections were first incubated at room temperature for 30 min in permeabilization buffer [1 % Triton and 0.1 % Tween20 in PBS] followed by 30 min in blocking solution [4 % FCS,0.3 % Triton and 0.05 % Tween20 in PBS]. Sections were then incubated for 24 h at room temperature under orbital agitation in rabbit anti NeuN (Millipore ab10807945, Cambridge, UK, Lot# ABN78, 1:500) diluted in blocking solution. After 3 × 10 min washes in blocking solution, slices were incubated in goat anti-rabbit-Alexa 488 (Thermofisher Scientific, Brisbane, Australia, 1:1000); diluted in blocking solution for 4 h at room temperature. Slices were then washed in PBS (3 × 10 min) followed by a 5 min incubation with DAPI (Thermofisher Scientific, 1: 5000) diluted in PBS. All sections were washed once with PBS for 5 min and mounted with Fluorescence Mounting Medium (Dako, Agilent, Santa Clara, California, USA). Images were acquired on a fluorescent slide scanner (Zeiss Axioscan, Zeiss, Sydney, Australia) with a 10x objective (1024 × 1024).

Immunohistochemistry of other tissues

Tissues were harvested and fixed in 4% paraformaldehyde for 24 h and then processed for paraffin-embedded histology using routine methods. Sections were deparaffinised and rehydrated in descending ethanol series. For H&E, 4 µm sections were stained with eosin and hematoxylin (Sigma-Aldrich) for 30 second and 1 minute respectively. For elastin staining, 4 µm sections were stained with Elastin solution, Weigert's iron hematoxylin solution and Picrofuchsin solution for 10, 5 and 2 minutes respectively (Elastin van Gieson staining kit, Merck, Melbourne, Australia). For Ki67 and IBA1 staining, epitope retrieval was performed by heat induction in 10 mM sodium citrate buffer pH 6.0. Sections were stained with rabbit anti-Ki67 (Abcam ab16667, Cambridge, UK, Lot# GR331319528, 1:1000) or rabbit anti-IBA1 (FUJIFILM, Wako Chemicals, Richmond, Virginia, USA, 019-19741, Lot# CAK1997, 1:1000). Secondary detection was with DAKO Envision anti-

rabbit HRP detection reagents (Agilent). Sections were then dehydrated in ascending ethanol series, clarified with xylene and mounted with DPX mountant (Sigma-Aldrich). Whole-slide digital imaging was performed on the VS120 Olympus slide scanner. DAB-positive areas were quantified using ImageJ (https://imagej.net/) in six different field per sample. For lung, DAB-positive areas were normalised to total number of cells per field**.**

RNA purification and qRT-PCR analysis

RNA was extracted using TRI Reagent (Sigma-Aldrich), according to manufacturer's instructions. For each extraction ~100 mg of tissue was processed using 1 ml reagent. Genomic DNA contamination of RNA preparations was eliminated by digestion with DNase I amplification grade (Thermofisher Scientific). RNA quantity was measured using a Nanodrop and RNA integrity estimated on an Agilent 2200 Tapestation System (Agilent). The RNA Integrity Number (RINe) was calculated for each sample and all samples used for sequencing had a RINe of ≥ 7.0.

Expression levels for selected genes were quantified using real-time PCR. cDNA was synthesized from 1 µg total RNA using cDNA synthesis kit (Bioline, Sydney, Australia) and RT-PCR was performed using the SYBR® Select Master Mix (Thermofisher Scientific) on an Applied Biosystems™ QuantStudio™ real-time PCR system (Thermofisher Scientific). Gene expression relative to *Hprt*, was calculated using the ΔCt method. Primer sequences: *Hprt* F: CTCAGTCCCAGCGTCGTGA, R: AACACCTTTTCCAAATCTTCAGCA; *Adgre1* F: GGGGCTATGGAATGCATAATCGC, R: AAGGAGGGCAGAGTTGATCGTG; *Csf1r* F: GACTGGAGAGGAGAGAGCAGGAC, R: CTGCCACCACCACTGTCACT.

Library preparation and sequencing

RNA-seq libraries were prepared by IMB Sequencing Facility, University of Queensland, Australia, with the TruSeq Stranded mRNA Library protocol (Illumina, San Diego, California, USA). Sequencing of 12 liver samples (with 84 unrelated samples) was performed using a single NovaSeq S1 200 cycle sequencing run on a NovaSeq 6000 machine (Illumina) through IMB Sequencing

Facility. Sequencing depth was between 9 million and 35 million paired end reads per sample. The raw sequencing data, in the form of .fastq files, are deposited in the European Nucleotide Archive under study accession number PRJEB39130.

Read pre-processing

Reads were pre-processed using fastp v0.20.0 [76] with parameters --length_required 50 --average_qual 10 --low_complexity_filter --correction --cut_right --cut_tail --cut_tail_window_size 1 --cut_tail_mean_quality 20. These parameters: (1) trim all bases from the 3' end that have quality < 20; (2) cut reads should the mean quality within a 4bp window, advanced 5' to 3', fall below 20; (3) require that 30% or more of the bases in each read are followed by a different base (an indicator of read complexity); (4) require a mean base quality across the entire read of > 10. By default, fastp also trims auto-detected adapters, discards reads with > 5 N (undetermined) bases, and requires that > 40% of the bases in each read have Phred score >15. Mismatched base pairs were corrected in regions of paired end reads that overlapped each other, should one base have a quality score higher than the other. This required a minimum overlap of 30bp, a difference in base qualities of 5, and no more than 20% of the bases in the overlapping region needing correction. Finally, we required a minimum read length of 50bp. Pre-processing discarded on average 8.5% of the bases per sample (Supplementary Table 1).

Expression quantification and differential gene expression analysis

For each set of cleaned reads, expression level was quantified as transcripts per million (TPM) using Kallisto v0.44.0 [77] with 100 bootstrap replicates. Kallisto quantifies expression by reference to an index of transcripts, which was constructed using the combined set of unique protein-coding transcripts from the Ensembl (ftp://ftp.ensembl.org/pub/release-98/fasta/rattus_norvegicus/cdna/Rattus_norvegicus.Rnor_6.0.cdna.all.fa.gz) and NCBI RefSeq (ftp://ftp.ncbi.nlm.nih.gov/genomes/all/GCF/000/001/895/GCF_000001895.5_Rnor_6.0/GCF_0000

01895.5_Rnor_6.0_rna.fna.gz) versions of the Rnor_6.0 annotation, as previously described (Bush et al., 2020) (n = 25,870 protein-coding genes in total, of which 22,238 had Ensembl IDs). Differential expression of genes comparing WT and *Csf1rko* was performed using Degust (https://degust.erc.monash.edu/). The FDR cut-off was 0.05, the method was Voom/Limma and only samples with a minimum read count of 1 TPM in at least one replicate were included.

Network analysis of gene expression

Network cluster analysis of gene expression in the livers of *Csf1rko* and WT rats was performed using BioLayout (http://biolayout.org). The expression levels determined by Kallisto were filtered to remove any gene where no sample reached 1 TPM. Similarities between expression profiles of individual samples (sample to sample analysis) or genes (gene to gene analysis) were determined by calculating a Pearson correlation matrix. For the sample to sample analysis, relationships where $r \geq 0.93$ (the highest r which included all 12 samples) were included. For the gene to gene analysis, the results were filtered to remove all relationships where $r < 0.95$. A network graph was constructed by connecting the remaining nodes (samples or genes) with edges (where the correlation coefficient between two samples or genes exceeded the threshold value). Samples or genes with similar expression patterns were located close to each other in the network. The gene to gene network graph was interpreted using the Markov Cluster Algorithm (MCL) at an inflation value (which determines cluster granularity) of 1.7. Genes with similar expression patterns were allocated to the same cluster, forming cliques of interconnected nodes. All results were verified using Spearman (non-parametric) correlation coefficient.

IGF1 and GH Immunoassay

Serum IGF1 was measured using Mouse/Rat DuoSet ELISA kit (R&D Systems, Minneapolis, Minnesota, USA) according to manufacturer instruction. GH was measured in rat serum as described previously [78]. Briefly, an ELISA plate was coated overnight at 4°C with capture antibody (National Institute of Diabetes and Digestive and Kidney Diseases (NIDDK)-anti-rat GH (rGH)-IC-1 (monkey),

AFP411S, NIDDK-National Hormone and Pituitary Program (NHPP, Torrance, California, USA) at a final dilution of 1:40,000. Non-specific binding was blocked using 5% skim milk in 0.05% PBS with Tween-20 for 2 hours. The bound protein was detected using rabbit anti-GH antibody at a final dilution of 1:40,000 (AFP5672099, NIDDK-NHPP) followed by horseradish peroxidase-conjugated antibody (anti-rabbit, IgG; GE Healthcare, Chicago, Illinois, USA) at a final dilution of 1:2000. The concentration of growth hormone was calculated by regression of the standard curve generated using a 2-fold serial dilution of mouse GH (mGH) (AFP-10783B, NIDDK-NHPP) in PBS-T supplemented with 0.2% BSA.

Glucose and Insulin measurements

Blood glucose and serum insulin were measured in non-fasted animals and in accordance with the manufacturer's instructions. Blood glucose was measured using a Sensocard glucometer and glucose strips (Point of Care Diagnostics, Sydney, Australia). Insulin levels were measured using a mouse and rat insulin ELISA (Mercodia, Uppsala, Sweden).

Quantitative measures of gut

Villi and crypt length and villi width in the small intestines of a mix of male and female *Csf1rko* (n=6) or WT (n=9) rats on the Dark Agouti background were measured as previously described [79]. 100-200 villi and crypts were analysed per rat ileal section and averaged for analysis. For quality control, only villi and crypts where a continuous epithelium from the base of the crypts to the tip of the villi could be measured were included in the analysis. For width analysis, total IBA^+ immunolabelling was also analysed in villus lamina propria (VLP), and the subepithelial dome (SED) and follicular-associated epithelium (FAE) of Peyer's patches (PP; 1-4 PP/rat). For submucosa and muscularis analysis, thickness for each was measured at 25 random spots on each rat ileal section.

TUNEL staining

TUNEL staining was performed using TACS® 2 TdT DAB (diaminobenzidine) Kit (Trevigen, Gaithersburg, Maryland, USA) according to manufacturer instruction.

Mammary gland wholemount

Mammary gland wholemounts were prepared using CUBIC-based tissue clearing and methyl green staining, as previously described [80]. Glands were imaged using an Olympus SZX10 stereo microscope. Exposure time was consistent between rat samples and brightness and contrast adjustment uniformly applied. Ductal and fat pad length were measured from the #4 mammary glands.

Mammary tissue immunohistochemistry

Immunostaining on formalin-fixed paraffin embedded rat mammary tissue was performed as previously described [81]. The following primary antibodies were used in this study: chicken anti-Krt5 (Biolegend, San Diego, California, USA; 905903, Lot# B279859, 1:1000), mouse anti-E-cadherin (BD Biosciences; 610182, Lot# 7292525, 1:400) and rabbit IBA1 (FUJIFILM Wako Chemicals; 019-19741, Lot# CAK1997, 1:1000). The following secondary antibodies (Thermofisher Scientific) were used in this study (1:500): goat anti-chicken AF488 (A11039), goat anti-mouse AF555 (A32727) and goat anti-rabbit AF647 (A21245). Nuclei were stained with DAPI dilactate (625 ng/mL) for 10 min. Tissue was imaged using an Olympus BX63F upright epifluorescence microscope. Brightness and contrast was optimally adjusted for lineage markers and DAPI. Exposure, brightness and contrast were kept consistent between tissue sections for IBA1.

Statistics

Statistical tests were performed using GraphPad Prism 7.03. Comparisons between WT and *Csf1rko* were performed using the unpaired Student's t-test or Mann-Whitney test as indicated in Figure Legends.

Acknowledgments

We would like to thank Ms. Lisa Foster (Manager, UQ Biological Resources) and her staff for assistance with breeding and husbandry of the *Csf1rko* rats. The generation of the *Csf1rko* rat was supported by UK Medical Research Council Grant MR/M019969/1 to DAH and CP. This work

was supported in part by Australian National Health and Medical Research Council (NHMRC) Grant GNT1163981 awarded to DAH and KMS. The laboratory is grateful for core support from The Mater Foundation. We acknowledge support from the Microscopy and Cytometry facilities of the Translational Research Institute (TRI). TRI is supported by the Australian Government.

References

References

1. Guilliams M, Thierry GR, Bonnardel J, Bajenoff M. Establishment and Maintenance of the Macrophage Niche. Immunity. 2020;52(3):434-51. Epub 2020/03/19. doi: 10.1016/j.immuni.2020.02.015. PubMed PMID: 32187515.

2. Hume DA, Irvine KM, Pridans C. The Mononuclear Phagocyte System: The Relationship between Monocytes and Macrophages. Trends Immunol. 2018. Epub 2018/12/24. doi: 10.1016/j.it.2018.11.007. PubMed PMID: 30579704.

3. Chitu V, Stanley ER. Regulation of Embryonic and Postnatal Development by the CSF-1 Receptor. Curr Top Dev Biol. 2017;123:229-75. Epub 2017/02/27. doi: 10.1016/bs.ctdb.2016.10.004. PubMed PMID: 28236968; PubMed Central PMCID: PMCPMC5479137.

4. Garceau V, Balic A, Garcia-Morales C, Sauter KA, McGrew MJ, Smith J, et al. The development and maintenance of the mononuclear phagocyte system of the chick is controlled by signals from the macrophage colony-stimulating factor receptor. BMC Biol. 2015;13:12. Epub 2015/04/11. doi: 10.1186/s12915-015-0121-9. PubMed PMID: 25857347; PubMed Central PMCID: PMCPMC4369834.

5. Garceau V, Smith J, Paton IR, Davey M, Fares MA, Sester DP, et al. Pivotal Advance: Avian colony-stimulating factor 1 (CSF-1), interleukin-34 (IL-34), and CSF-1 receptor genes and gene products. J Leukoc Biol. 2010;87(5):753-64. Epub 2010/01/07. doi: 10.1189/jlb.0909624. PubMed PMID: 20051473.

6. Hume DA, Caruso M, Ferrari-Cestari M, Summers KM, Pridans C, Irvine KM. Phenotypic impacts of CSF1R deficiencies in humans and model organisms. J Leukoc Biol. 2020;107(2):205-19. Epub 2019/07/23. doi: 10.1002/JLB.MR0519-143R. PubMed PMID: 31330095.

7. Wynn TA, Chawla A, Pollard JW. Macrophage biology in development, homeostasis and disease. Nature. 2013;496(7446):445-55. Epub 2013/04/27. doi: 10.1038/nature12034. PubMed PMID: 23619691; PubMed Central PMCID: PMCPMC3725458.

8. Guo L, Bertola DR, Takanohashi A, Saito A, Segawa Y, Yokota T, et al. Bi-allelic CSF1R Mutations Cause Skeletal Dysplasia of Dysosteosclerosis-Pyle Disease Spectrum and Degenerative Encephalopathy with Brain Malformation. Am J Hum Genet. 2019;104(5):925-35. Epub 2019/04/16. doi: 10.1016/j.ajhg.2019.03.004. PubMed PMID: 30982609.

9. Oosterhof N, Kuil LE, van der Linde HC, Burm SM, Berdowski W, van Ijcken WFJ, et al. Colony-Stimulating Factor 1 Receptor (CSF1R) Regulates Microglia Density and Distribution, but Not Microglia Differentiation In Vivo. Cell Rep. 2018;24(5):1203-17 e6. Epub 2018/08/02. doi: 10.1016/j.celrep.2018.06.113. PubMed PMID: 30067976.

10. Pridans C, Raper A, David GM, Alves J, Sauter KA, Lefevre L, et al. Pleiotropic Impacts of Macrophage and Microglial Deficiency on Development in Rats with Targeted Mutation of the Csf1r Locus. JImmunol. 2018;201(9):2683-99.

11. Bennett FC, Bennett ML, Yaqoob F, Mulinyawe SB, Grant GA, Hayden Gephart M, et al. A Combination of Ontogeny and CNS Environment Establishes Microglial Identity. Neuron. 2018;98(6):1170-83 e8. Epub 2018/06/05. doi: 10.1016/j.neuron.2018.05.014. PubMed PMID: 29861285; PubMed Central PMCID: PMCPMC6023731.

12. Erblich B, Zhu L, Etgen AM, Dobrenis K, Pollard JW. Absence of colony stimulation factor-1 receptor results in loss of microglia, disrupted brain development and olfactory deficits. PLoS One. 2011;6(10):e26317. Epub 2011/11/03. doi: 10.1371/journal.pone.0026317. PubMed PMID: 22046273; PubMed Central PMCID: PMCPMC3203114.

13. Albertoni Borghese MF, Ortiz MC, Balonga S, Moreira Szokalo R, Majowicz MP. The Role of Endothelin System in Renal Structure and Function during the Postnatal Development

of the Rat Kidney. PLoS One. 2016;11(2):e0148866. Epub 2016/02/13. doi: 10.1371/journal.pone.0148866. PubMed PMID: 26872270; PubMed Central PMCID: PMCPMC4752218.

14. Sehgal A, Donaldson DS, Pridans C, Sauter KA, Hume DA, Mabbott NA. The role of CSF1R-dependent macrophages in control of the intestinal stem-cell niche. Nat Commun. 2018;9(1):1272. Epub 2018/03/30. doi: 10.1038/s41467-018-03638-6. PubMed PMID: 29593242; PubMed Central PMCID: PMCPMC5871851.

15. Ingman WV, Wyckoff J, Gouon-Evans V, Condeelis J, Pollard JW. Macrophages promote collagen fibrillogenesis around terminal end buds of the developing mammary gland. Dev Dyn. 2006;235(12):3222-9. Epub 2006/10/10. doi: 10.1002/dvdy.20972. PubMed PMID: 17029292.

16. Van Nguyen A, Pollard JW. Colony stimulating factor-1 is required to recruit macrophages into the mammary gland to facilitate mammary ductal outgrowth. Dev Biol. 2002;247(1):11-25. Epub 2002/06/21. doi: 10.1006/dbio.2002.0669. PubMed PMID: 12074549.

17. Irvine KM, Caruso M, Ferrari Cestari M, Davis GM, Pridans C, Keshvari S, et al. Analysis of the impact of Colony Stimulating Factor (CSF1)-1 administration in adult rats using a novel Csf1r-mApple reporter gene. Jounral of Leukocyte Biology. 2019;Under review.

18. MacDonald KP, Palmer JS, Cronau S, Seppanen E, Olver S, Raffelt NC, et al. An antibody against the colony-stimulating factor 1 receptor depletes the resident subset of monocytes and tissue- and tumor-associated macrophages but does not inhibit inflammation. Blood. 2010;116(19):3955-63. Epub 2010/08/05. doi: 10.1182/blood-2010-02-266296. PubMed PMID: 20682855.

19. Yona S, Kim KW, Wolf Y, Mildner A, Varol D, Breker M, et al. Fate mapping reveals origins and dynamics of monocytes and tissue macrophages under homeostasis. Immunity.

2013;38(1):79-91. Epub 2013/01/01. doi: 10.1016/j.immuni.2012.12.001. PubMed PMID: 23273845; PubMed Central PMCID: PMCPMC3908543.

20. Kohler C. Allograft inflammatory factor-1/Ionized calcium-binding adapter molecule 1 is specifically expressed by most subpopulations of macrophages and spermatids in testis. Cell Tissue Res. 2007;330(2):291-302. Epub 2007/09/18. doi: 10.1007/s00441-007-0474-7. PubMed PMID: 17874251.

21. Ito D, Imai Y, Ohsawa K, Nakajima K, Fukuuchi Y, Kohsaka S. Microglia-specific localisation of a novel calcium binding protein, Iba1. Brain Res Mol Brain Res. 1998;57(1):1-9. Epub 1998/06/19. doi: 10.1016/s0169-328x(98)00040-0. PubMed PMID: 9630473.

22. Pervin M, Golbar HM, Bondoc A, Izawa T, Kuwamura M, Yamate J. Immunophenotypical characterization and influence on liver homeostasis of depleting and repopulating hepatic macrophages in rats injected with clodronate. Exp Toxicol Pathol. 2016;68(2-3):113-24. Epub 2015/11/28. doi: 10.1016/j.etp.2015.11.003. PubMed PMID: 26610753.

23. Henson PM, Hume DA. Apoptotic cell removal in development and tissue homeostasis. Trends Immunol. 2006;27(5):244-50. Epub 2006/04/06. doi: 10.1016/j.it.2006.03.005. PubMed PMID: 16584921.

24. Lichanska AM, Browne CM, Henkel GW, Murphy KM, Ostrowski MC, McKercher SR, et al. Differentiation of the mononuclear phagocyte system during mouse embryogenesis: the role of transcription factor PU.1. Blood. 1999;94(1):127-38. Epub 1999/06/25. PubMed PMID: 10381505.

25. Irvine KM, Caruso M, Cestari MF, Davis GM, Keshvari S, Sehgal A, et al. Analysis of the impact of CSF-1 administration in adult rats using a novel Csf1r-mApple reporter gene. J Leukoc Biol. 2020;107(2):221-35. Epub 2019/08/10. doi: 10.1002/JLB.MA0519-149R. PubMed PMID: 31397014.

26. Hume DA, Gordon S. Mononuclear phagocyte system of the mouse defined by immunohistochemical localization of antigen F4/80. Identification of resident macrophages in renal medullary and cortical interstitium and the juxtaglomerular complex. J Exp Med. 1983;157(5):1704-9. Epub 1983/05/01. doi: 10.1084/jem.157.5.1704. PubMed PMID: 6854206; PubMed Central PMCID: PMCPMC2186998.

27. Mossadegh-Keller N, Gentek R, Gimenez G, Bigot S, Mailfert S, Sieweke MH. Developmental origin and maintenance of distinct testicular macrophage populations. J Exp Med. 2017;214(10):2829-41. Epub 2017/08/09. doi: 10.1084/jem.20170829. PubMed PMID: 28784628; PubMed Central PMCID: PMCPMC5626405.

28. Kishikawa S, Sato S, Kaneto S, Uchino S, Kohsaka S, Nakamura S, et al. Allograft inflammatory factor 1 is a regulator of transcytosis in M cells. Nat Commun. 2017;8:14509. Epub 2017/02/23. doi: 10.1038/ncomms14509. PubMed PMID: 28224999; PubMed Central PMCID: PMCPMC5322540.

29. Dai XM, Ryan GR, Hapel AJ, Dominguez MG, Russell RG, Kapp S, et al. Targeted disruption of the mouse colony-stimulating factor 1 receptor gene results in osteopetrosis, mononuclear phagocyte deficiency, increased primitive progenitor cell frequencies, and reproductive defects. Blood. 2002;99(1):111-20. Epub 2002/01/05. doi: 10.1182/blood.v99.1.111. PubMed PMID: 11756160.

30. Guilliams M, De Kleer I, Henri S, Post S, Vanhoutte L, De Prijck S, et al. Alveolar macrophages develop from fetal monocytes that differentiate into long-lived cells in the first week of life via GM-CSF. J Exp Med. 2013;210(10):1977-92. Epub 2013/09/18. doi: 10.1084/jem.20131199. PubMed PMID: 24043763; PubMed Central PMCID: PMCPMC3782041.

31. Guler HP, Zapf J, Scheiwiller E, Froesch ER. Recombinant human insulin-like growth factor I stimulates growth and has distinct effects on organ size in hypophysectomized rats.

Proc Natl Acad Sci U S A. 1988;85(13):4889-93. Epub 1988/07/01. doi: 10.1073/pnas.85.13.4889. PubMed PMID: 3387445; PubMed Central PMCID: PMCPMC280542.

32. Lupu F, Terwilliger JD, Lee K, Segre GV, Efstratiadis A. Roles of growth hormone and insulin-like growth factor 1 in mouse postnatal growth. Dev Biol. 2001;229(1):141-62. Epub 2001/01/03. doi: 10.1006/dbio.2000.9975. PubMed PMID: 11133160.

33. Kineman RD, Del Rio-Moreno M, Sarmento-Cabral A. 40 YEARS of IGF1: Understanding the tissue-specific roles of IGF1/IGF1R in regulating metabolism using the Cre/loxP system. J Mol Endocrinol. 2018;61(1):T187-T98. Epub 2018/05/11. doi: 10.1530/JME-18-0076. PubMed PMID: 29743295.

34. Duran-Ortiz S, Noboa V, Kopchick JJ. Tissue-specific disruption of the growth hormone receptor (GHR) in mice: An update. Growth Horm IGF Res. 2020;51:1-5. Epub 2020/01/11. doi: 10.1016/j.ghir.2019.12.004. PubMed PMID: 31923746.

35. Gow DJ, Sauter KA, Pridans C, Moffat L, Sehgal A, Stutchfield BM, et al. Characterisation of a novel Fc conjugate of macrophage colony-stimulating factor. Mol Ther. 2014;22(9):1580-92. Epub 2014/06/26. doi: 10.1038/mt.2014.112. PubMed PMID: 24962162; PubMed Central PMCID: PMCPMC4435485.

36. Sauter KA, Waddell LA, Lisowski ZM, Young R, Lefevre L, Davis GM, et al. Macrophage colony-stimulating factor (CSF1) controls monocyte production and maturation and the steady-state size of the liver in pigs. Am J Physiol Gastrointest Liver Physiol. 2016;311(3):G533-47. Epub 2016/07/23. doi: 10.1152/ajpgi.00116.2016. PubMed PMID: 27445344; PubMed Central PMCID: PMCPMC5076001.

37. Alexander B, Guzail MA, Foster CS. Morphological changes during hepatocellular maturity in neonatal rats. Anat Rec. 1997;248(1):104-9. Epub 1997/05/01. doi:

10.1002/(SICI)1097-0185(199705)248:1<104::AID-AR12>3.0.CO;2-T. PubMed PMID: 9143673.

38. Septer S, Edwards G, Gunewardena S, Wolfe A, Li H, Daniel J, et al. Yes-associated protein is involved in proliferation and differentiation during postnatal liver development. Am J Physiol Gastrointest Liver Physiol. 2012;302(5):G493-503. Epub 2011/12/24. doi: 10.1152/ajpgi.00056.2011. PubMed PMID: 22194415; PubMed Central PMCID: PMCPMC3311431.

39. Marquez MG, Cabrera I, Serrano DJ, Sterin-Speziale N. Cell proliferation and morphometric changes in the rat kidney during postnatal development. Anat Embryol (Berl). 2002;205(5-6):431-40. Epub 2002/10/17. doi: 10.1007/s00429-002-0262-9. PubMed PMID: 12382146.

40. Bolle I, Eder G, Takenaka S, Ganguly K, Karrasch S, Zeller C, et al. Postnatal lung function in the developing rat. J Appl Physiol (1985). 2008;104(4):1167-76. Epub 2008/01/12. doi: 10.1152/japplphysiol.00587.2007. PubMed PMID: 18187616.

41. Lichanska AM, Waters MJ. How growth hormone controls growth, obesity and sexual dimorphism. Trends Genet. 2008;24(1):41-7. Epub 2007/12/08. doi: 10.1016/j.tig.2007.10.006. PubMed PMID: 18063438.

42. Pridans C, Sauter KA, Irvine KM, Davis GM, Lefevre L, Raper A, et al. Macrophage colony-stimulating factor increases hepatic macrophage content, liver growth, and lipid accumulation in neonatal rats. Am J Physiol Gastrointest Liver Physiol. 2018;314(3):G388-G98. Epub 2018/01/20. doi: 10.1152/ajpgi.00343.2017. PubMed PMID: 29351395; PubMed Central PMCID: PMCPMC5899243.

43. Banaei-Bouchareb L, Gouon-Evans V, Samara-Boustani D, Castellotti MC, Czernichow P, Pollard JW, et al. Insulin cell mass is altered in Csf1op/Csf1op macrophage-

deficient mice. J Leukoc Biol. 2004;76(2):359-67. Epub 2004/06/05. doi: 10.1189/jlb.1103591. PubMed PMID: 15178709.

44. Bush SJ, McCulloch MEB, Lisowski ZM, Muriuki C, Clark EL, Young R, et al. Species-Specificity of Transcriptional Regulation and the Response to Lipopolysaccharide in Mammalian Macrophages. Front Cell Dev Biol. 2020;8:661. Epub 2020/08/15. doi: 10.3389/fcell.2020.00661. PubMed PMID: 32793601; PubMed Central PMCID: PMCPMC7386301.

45. Summers KM, Hume DA. Identification of the macrophage-specific promoter signature in FANTOM5 mouse embryo developmental time course data. J Leukoc Biol. 2017;102(4):1081-92. Epub 2017/07/29. doi: 10.1189/jlb.1A0417-150RR. PubMed PMID: 28751473.

46. Vannella KM, Wynn TA. Mechanisms of Organ Injury and Repair by Macrophages. Annu Rev Physiol. 2017;79:593-617. Epub 2016/12/14. doi: 10.1146/annurev-physiol-022516-034356. PubMed PMID: 27959618.

47. Summers KM, Bush SJ, Hume DA. Transcriptional network analysis of transcriptomic diversity in resident tissue macrophages and dendritic cells in the mouse mononuclear phagocyte system. BioRxiv. 2020;03.24.:002816.

48. Chang HR, Kim HJ, Xu X, Ferrante AW, Jr. Macrophage and adipocyte IGF1 maintain adipose tissue homeostasis during metabolic stresses. Obesity (Silver Spring). 2016;24(1):172-83. Epub 2015/12/15. doi: 10.1002/oby.21354. PubMed PMID: 26663512; PubMed Central PMCID: PMCPMC4793714.

49. Mass E, Ballesteros I, Farlik M, Halbritter F, Gunther P, Crozet L, et al. Specification of tissue-resident macrophages during organogenesis. Science. 2016;353(6304). Epub 2016/08/06. doi: 10.1126/science.aaf4238. PubMed PMID: 27492475; PubMed Central PMCID: PMCPMC5066309.

50. Scott CL, Zheng F, De Baetselier P, Martens L, Saeys Y, De Prijck S, et al. Bone marrow-derived monocytes give rise to self-renewing and fully differentiated Kupffer cells. Nat Commun. 2016;7:10321. Epub 2016/01/28. doi: 10.1038/ncomms10321. PubMed PMID: 26813785; PubMed Central PMCID: PMCPMC4737801.

51. Michalopoulos GK. Hepatostat: Liver regeneration and normal liver tissue maintenance. Hepatology. 2017;65(4):1384-92. Epub 2016/12/21. doi: 10.1002/hep.28988. PubMed PMID: 27997988.

52. Stutchfield BM, Antoine DJ, Mackinnon AC, Gow DJ, Bain CC, Hawley CA, et al. CSF1 Restores Innate Immunity After Liver Injury in Mice and Serum Levels Indicate Outcomes of Patients With Acute Liver Failure. Gastroenterology. 2015;149(7):1896-909 e14. Epub 2015/09/08. doi: 10.1053/j.gastro.2015.08.053. PubMed PMID: 26344055; PubMed Central PMCID: PMCPMC4672154.

53. Behrens A, Sibilia M, David JP, Mohle-Steinlein U, Tronche F, Schutz G, et al. Impaired postnatal hepatocyte proliferation and liver regeneration in mice lacking c-jun in the liver. EMBO J. 2002;21(7):1782-90. Epub 2002/04/03. doi: 10.1093/emboj/21.7.1782. PubMed PMID: 11927562; PubMed Central PMCID: PMCPMC125360.

54. Peinado-Onsurbe J, Staels B, Deeb S, Ramirez I, Llobera M, Auwerx J. Neonatal extinction of liver lipoprotein lipase expression. Biochim Biophys Acta. 1992;1131(3):281-6. Epub 1992/07/15. doi: 10.1016/0167-4781(92)90026-v. PubMed PMID: 1627643.

55. Kammerer L, Mohammad GH, Wolna M, Robbins P, Lakhal-Littleton S. Fetal liver hepcidin secures iron stores in utero. Blood. 2020. Epub 2020/06/17. doi: 10.1182/blood.2019003907. PubMed PMID: 32542311.

56. Cramer S, Beveridge M, Kilberg M, Novak D. Physiological importance of system A-mediated amino acid transport to rat fetal development. Am J Physiol Cell Physiol.

2002;282(1):C153-60. Epub 2001/12/18. doi: 10.1152/ajpcell.2002.282.1.C153. PubMed PMID: 11742808.

57. Fuhrmeister J, Zota A, Sijmonsma TP, Seibert O, Cingir S, Schmidt K, et al. Fasting-induced liver GADD45beta restrains hepatic fatty acid uptake and improves metabolic health. EMBO Mol Med. 2016;8(6):654-69. Epub 2016/05/04. doi: 10.15252/emmm.201505801. PubMed PMID: 27137487; PubMed Central PMCID: PMCPMC4888855.

58. Shi H, Yao R, Lian S, Liu P, Liu Y, Yang YY, et al. Regulating glycolysis, the TLR4 signal pathway and expression of RBM3 in mouse liver in response to acute cold exposure. Stress. 2019;22(3):366-76. Epub 2019/03/02. doi: 10.1080/10253890.2019.1568987. PubMed PMID: 30821572.

59. Adams JM, Otero-Corchon V, Hammond GL, Veldhuis JD, Qi N, Low MJ. Somatostatin is essential for the sexual dimorphism of GH secretion, corticosteroid-binding globulin production, and corticosterone levels in mice. Endocrinology. 2015;156(3):1052-65. Epub 2015/01/01. doi: 10.1210/en.2014-1429. PubMed PMID: 25551181; PubMed Central PMCID: PMCPMC4330306.

60. Martinez-Jimenez CP, Kyrmizi I, Cardot P, Gonzalez FJ, Talianidis I. Hepatocyte nuclear factor 4alpha coordinates a transcription factor network regulating hepatic fatty acid metabolism. Mol Cell Biol. 2010;30(3):565-77. Epub 2009/11/26. doi: 10.1128/MCB.00927-09. PubMed PMID: 19933841; PubMed Central PMCID: PMCPMC2812226.

61. Gold EJ, Zhang X, Wheatley AM, Mellor SL, Cranfield M, Risbridger GP, et al. betaA- and betaC-activin, follistatin, activin receptor mRNA and betaC-activin peptide expression during rat liver regeneration. J Mol Endocrinol. 2005;34(2):505-15. Epub 2005/04/12. doi: 10.1677/jme.1.01657. PubMed PMID: 15821113.

62. Percival CJ, Richtsmeier JT. Angiogenesis and intramembranous osteogenesis. Dev Dyn. 2013;242(8):909-22. Epub 2013/06/06. doi: 10.1002/dvdy.23992. PubMed PMID: 23737393; PubMed Central PMCID: PMCPMC3803110.

63. Opperman LA. Cranial sutures as intramembranous bone growth sites. Dev Dyn. 2000;219(4):472-85. Epub 2000/11/21. doi: 10.1002/1097-0177(2000)9999:9999<::AID-DVDY1073>3.0.CO;2-F. PubMed PMID: 11084647.

64. Chang MK, Raggatt LJ, Alexander KA, Kuliwaba JS, Fazzalari NL, Schroder K, et al. Osteal tissue macrophages are intercalated throughout human and mouse bone lining tissues and regulate osteoblast function in vitro and in vivo. J Immunol. 2008;181(2):1232-44. Epub 2008/07/09. doi: 10.4049/jimmunol.181.2.1232. PubMed PMID: 18606677.

65. Alexander KA, Chang MK, Maylin ER, Kohler T, Muller R, Wu AC, et al. Osteal macrophages promote in vivo intramembranous bone healing in a mouse tibial injury model. J Bone Miner Res. 2011;26(7):1517-32. Epub 2011/02/10. doi: 10.1002/jbmr.354. PubMed PMID: 21305607.

66. Batoon L, Millard SM, Wullschleger ME, Preda C, Wu AC, Kaur S, et al. CD169(+) macrophages are critical for osteoblast maintenance and promote intramembranous and endochondral ossification during bone repair. Biomaterials. 2019;196:51-66. Epub 2017/11/07. doi: 10.1016/j.biomaterials.2017.10.033. PubMed PMID: 29107337.

67. Lazarus S, Tseng HW, Lawrence F, Woodruff MA, Duncan EL, Pettit AR. Characterization of Normal Murine Carpal Bone Development Prompts Re-Evaluation of Pathologic Osteolysis as the Cause of Human Carpal-Tarsal Osteolysis Disorders. Am J Pathol. 2017;187(9):1923-34. Epub 2017/07/05. doi: 10.1016/j.ajpath.2017.05.007. PubMed PMID: 28675805.

68. Sobacchi C, Schulz A, Coxon FP, Villa A, Helfrich MH. Osteopetrosis: genetics, treatment and new insights into osteoclast function. Nat Rev Endocrinol. 2013;9(9):522-36. Epub 2013/07/24. doi: 10.1038/nrendo.2013.137. PubMed PMID: 23877423.

69. Rojo R, Raper A, Ozdemir DD, Lefevre L, Grabert K, Wollscheid-Lengeling E, et al. Deletion of a Csf1r enhancer selectively impacts CSF1R expression and development of tissue macrophage populations. Nat Commun. 2019;10(1):3215. Epub 2019/07/22. doi: 10.1038/s41467-019-11053-8. PubMed PMID: 31324781; PubMed Central PMCID: PMCPMC6642117.

70. Kaur S, Raggatt LJ, Batoon L, Hume DA, Levesque JP, Pettit AR. Role of bone marrow macrophages in controlling homeostasis and repair in bone and bone marrow niches. Semin Cell Dev Biol. 2017;61:12-21. Epub 2016/08/16. doi: 10.1016/j.semcdb.2016.08.009. PubMed PMID: 27521519.

71. Kaur S, Raggatt LJ, Millard SM, Wu AC, Batoon L, Jacobsen RN, et al. Self-repopulating recipient bone marrow resident macrophages promote long-term hematopoietic stem cell engraftment. Blood. 2018;132(7):735-49. Epub 2018/06/28. doi: 10.1182/blood-2018-01-829663. PubMed PMID: 29945953.

72. Hettinger J, Richards DM, Hansson J, Barra MM, Joschko AC, Krijgsveld J, et al. Origin of monocytes and macrophages in a committed progenitor. Nat Immunol. 2013;14(8):821-30. Epub 2013/07/03. doi: 10.1038/ni.2638. PubMed PMID: 23812096.

73. Grabert K, Sehgal A, Irvine KM, Wollscheid-Lengeling E, Ozdemir DD, Stables J, et al. A mouse transgenic line that reports CSF1R protein expression provides a definitive differentiation marker for the mouse mononuclear phagocyte system. J Immunol 2020;In press.

74. Gelfand JM, Greenfield AL, Barkovich M, Mendelsohn BA, Van Haren K, Hess CP, et al. Allogeneic HSCT for adult-onset leukoencephalopathy with spheroids and pigmented

glia. Brain. 2020;143(2):503-11. Epub 2019/12/17. doi: 10.1093/brain/awz390. PubMed PMID: 31840744.

75. Wallin J, Wilting J, Koseki H, Fritsch R, Christ B, Balling R. The role of Pax-1 in axial skeleton development. Development. 1994;120(5):1109-21. Epub 1994/05/01. PubMed PMID: 8026324.

76. Chen S, Zhou Y, Chen Y, Gu J. fastp: an ultra-fast all-in-one FASTQ preprocessor. Bioinformatics. 2018;34(17):i884-i90. Epub 2018/11/14. doi: 10.1093/bioinformatics/bty560. PubMed PMID: 30423086; PubMed Central PMCID: PMCPMC6129281.

77. Bray NL, Pimentel H, Melsted P, Pachter L. Near-optimal probabilistic RNA-seq quantification. Nat Biotechnol. 2016;34(5):525-7. Epub 2016/04/05. doi: 10.1038/nbt.3519. PubMed PMID: 27043002.

78. Steyn FJ, Huang L, Ngo ST, Leong JW, Tan HY, Xie TY, et al. Development of a method for the determination of pulsatile growth hormone secretion in mice. Endocrinology. 2011;152(8):3165-71. Epub 2011/05/19. doi: 10.1210/en.2011-0253. PubMed PMID: 21586549.

79. Sauter KA, Pridans C, Sehgal A, Tsai YT, Bradford BM, Raza S, et al. Pleiotropic effects of extended blockade of CSF1R signaling in adult mice. J Leukoc Biol. 2014;96(2):265-74. Epub 2014/03/22. doi: 10.1189/jlb.2A0114-006R. PubMed PMID: 24652541; PubMed Central PMCID: PMCPMC4378363.

80. Lloyd-Lewis B, Davis FM, Harris OB, Hitchcock JR, Lourenco FC, Pasche M, et al. Imaging the mammary gland and mammary tumours in 3D: optical tissue clearing and immunofluorescence methods. Breast Cancer Res. 2016;18(1):127. Epub 2016/12/15. doi: 10.1186/s13058-016-0754-9. PubMed PMID: 27964754; PubMed Central PMCID: PMCPMC5155399.

81. Davis FM, Lloyd-Lewis B, Harris OB, Kozar S, Winton DJ, Muresan L, et al. Single-cell lineage tracing in the mammary gland reveals stochastic clonal dispersion of stem/progenitor cell progeny. Nat Commun. 2016;7:13053. Epub 2016/10/26. doi: 10.1038/ncomms13053. PubMed PMID: 27779190; PubMed Central PMCID: PMCPMC5093309.

Figure legends:

Figure 1. Postnatal skeletal development in *Csf1rko* rats.

(A) Representative 3D reconstruction of micro-CT images in newborn (Week 0) and 1wk old WT and *Csf1rko* rats. Digits of forepaws in white boxes. (B) Alcian blue and Alizarin red staining of newborn WT and *Csf1rko* rats with ossified cartilage/bone stained red (black arrows) and unossified cartilage/bone stained blue. (C) Representative 3D reconstructed micro-CT images of 3-week old rat ribcage (left panel) and hind paw (right panel) with arrow heads indicating variance in ossification in distal metatarsal/proximal phalanges. (D) Representative 3D reconstructed micro-CT images of 7-wk old rat skull of WT (top) and *Csf1rko* (bottom) rats. (E) Representative images of laminin staining of hindlimb muscles of WT and *Csf1rko* rats at 1, 3 and 7 wks. (F) Average diameter of muscle fibres from the posterior tibialis in WT and *Csf1rko* rats at 3 wks. Original magnification: 400X. Scale bar: 20 µm.

Figure 2. Flow cytometric analysis of peripheral blood and bone marrow leukocytes.

(A) Flow cytometry gating strategy to distinguish (i) CD172A+ myeloid cells, (ii) $HIS48^{+}/SSC^{Hi}$ granulocytes among myeloid cells, (iii) HIS48 and CD43-expressing monocyte subsets among non-granulocyte myeloid cells and (iv) $CD45R^{+}$ B cells among $CD172A^{-}$ lymphocytes. (B-D) Quantification of peripheral blood granulocytes (B), monocyte subsets (C) and B cells (D) in WT and *Csf1rko* rats at 3 and 9 wks of age. (E) Bone marrow flow cytometry gating strategy to distinguish (i) $HIS48^{+}/SSC^{Hi}$ granulocytes, (ii) $CD172^{+}$ and $CD172^{Low}/CD4^{Int}$ monocytes/macrophages among non-granulocytes, (iii) monocyte/macrophage subsets and (iv) CD45R+ B cells among CD172A-/CD4- cells. (F-H) Quantification of BM granulocytes (F), monocyte/macrophage subsets (G) and B cells (H). All genotype comparisons were analysed by Mann Whitney test.

Figure 3. IBA1 expression and TUNEL staining in WT and *Csf1rko* embryos.

(A) Histological analysis of IBA1 expression in embryos of WT and *Csf1rko* from the same litter approximately 10.5 days post conception (dpc). IBA1+ cells are detectable through the WT embryo

and absent from the *Csf1rko*. The fetal liver (squares) is shown at higher magnification in the lower panels. Note that early digit condensation is evident in the hind limb of the *Csf1rko* embryo but there are no infiltrating IBA1$^+$ cells (B) TUNEL staining in the liver of WT and *Csf1rko* embryos approximately 10.5 dpc. TUNEL$^+$ expelled nuclei retained in the *Csf1rko* liver are highlighted by red arrows.

Figure 4. Immunolocalization of IBA1$^+$ cells in WT and *Csf1rko* rat organs at 3 wks.

(A-D) Representative images of immunohistochemical localisation of IBA1 in (A) kidney, (B) testes and seminal vesicles, (C) ileum including Peyer's patches and (D) liver and lung of WT and *Csf1rko* rats. M cells in the follicle-associated epithelium are indicated by red arrows. Black arrowheads highlight IBA1$^+$ cells in the base of the crypts in (C). (E-G) Quantitative analysis of IBA1+ cells in (E) liver, (F) kidney and (G) lung. n ≥ 6 per genotype, graphs show the mean ± SD, genotype comparisons were analysed by Mann Whitney test.

Figure 5. Immunolocalization of IBA1$^+$ cells in WT and *Csf1rko* rat organs at 7 wks. Representative images of immunohistochemical localisation of IBA1 in (A) kidney, (B) testes and seminal vesicles, (C) small intestine including Peyer's patches, (D) lung and heart and (E) liver and spleen of WT and *Csf1rko* rats. M cells in small intestine are indicated by red arrows in (C). Black arrowheads highlight IBA1$^+$ cells in the base of the crypts in (C).

Figure 6. Detection of Ki67$^+$ proliferating cells in the liver, kidney and lung of WT and *Csf1rko* rats at 3 wks of age.

(A-C) Representative images of Ki67 staining in (A) liver, (B) kidney and (C) lung of WT and *Csf1rko* rats. D-F) Quantitative analysis of Ki67+ cells in (D) liver, (E) kidney and (F) lung. n ≥ 6 per genotype, graphs shows the mean ± SD, genotype comparisons were analysed by Mann Whitney test.

Figure 7. Analysis of gene expression in livers of WT and *Csf1rko* rats.

RNA-seq analysis was performed on liver from 3 male and 3 female wild-type and *Csf1rko* rats at 3 wks of age. The full data set and the differentially-expressed gene analysis are provided in Table S1A and S1B. Co-expression cluster analysis was performed using BioLayout as described in Materials and Methods. (A) Summary of regulated genes. Genes shown were regulated >2 fold in the livers of *Csf1rko* rats compared to WT. They have been assigned to categories based upon known function or expression. Genes in red encode proteins that inhibit liver or somatic growth and are over-expressed in the *Csf1rko*. (B) Sample to sample analysis of *Csf1rko* and wild type liver samples. Circles represent samples and lines between them show correlations of $r \geq 0.93$ between expression patterns of pairs of samples across all genes. (C) Average expression profile of four clusters of co-expressed transcripts generated using BioLayout that distinguish *Csf1rko* and wild-type liver. Full list of transcripts within each cluster is provided in Table S1C and GO annotation in Table S1D. Y axis shows the average expression of transcripts in the cluster (TPM); X axis shows the samples with columns colored as for (B).

Figure 8. Histological analysis of lipid accumulation in the liver and quantitative measures of blood glucose and serum insulin.

(A) Representative images of H&E staining in the liver of WT (top panel) and *Csf1rko* (bottom panel) rats at 3 wks (left panels), 7 wks (middle panels) and 12 wks (right panels). (B) Blood glucose and (C) serum insulin levels measured at 3 wks in WT and *Csf1rko* rats. $n \geq 6$ per genotype, graphs show the mean ± SD, genotype comparisons were analysed by Mann Whitney test.

Figure 9. *Csf1rko* phenotype rescue by WT BM transfer.

A cohort of 9 female and 2 male *Csf1rko* rats was treated by BM transfer at 3 wks of age. (A) Time course of body weight gain in female WT ($n \geq 3$) *Csf1rko* rats with WT bone marrow transfer (BMT) and *Csf1rko* from 3 wks of age to harvest. Note that *Csf1rko* rats were euthanised at 11-12 wks for welfare reasons. (B) Serum IGF-1 levels and (C) serum growth hormone (GH) levels in a mixed cohort of male and female WT, *Csf1rko* following bone marrow transfer at 3 wks (BMT) and *Csf1rko*

rats at the ages indicated. (D, E) qRT-PCR analysis of liver (D) *Csf1r* and (E) *Adgre1* expression in 3-, 7- and 12-wks old WT, *Csf1rko* (BMT) *and Csf1rko* rats. n ≥ 3 per genotype, graphs show the mean ± SD. (F-H) Representative 3D reconstructed micro-CT images of WT, *Csf1rko* and *Csf1rko* (BMT) rat hind limbs (F), hind paws (G) and skulls (H) comparing medulla cavity (arrows), ossification of phalanges (white arrowheads) and closure of cranial sutures (black arrowheads). (I) representative images of H&E staining in the liver at 7 and 12 wks of age of *Csf1rko* (BMT) rats after WT bone marrow transfer.

Figure 10. Analysis of the effect of bone marrow transfer at 3 wks of age on peritoneal, peripheral blood and bone marrow leukocyte populations in *Csf1rko* rats.

(A) Flow cytometry gating strategy to identify peritoneal granulocytes and macrophages. (B, C) Flow cytometric analysis of peritoneal granulocytes (B) and macrophages (C) in *Csf1rko* rats 9 wks post bone marrow transfer at 3 wks of age compared to age-matched WT controls. (D-F) Flow cytometric analysis of peripheral blood (D) monocyte subsets, (E) granulocytes and (F) B cells in *Csf1rko* rats 9 wks post bone marrow transfer at 3 wks of age compared to age-matched WT controls. (G-H) Flow cytometric analysis of bone marrow (BM) (G) monocyte/macrophage subsets, (H) granulocytes and (I) B cells in *Csf1rko* rats 9 wks post bone marrow transfer at 3 wks of age compared to age-matched WT controls. (J) BM from WT and *Csf1rko* rats shown in panels G-H was cultured for 7 days in 100 ng/ml CSF1 to generate bone marrow-derived macrophages. Representative images of cultures from 5 separate animals (scale bar 50 uM). All genotype comparisons were analysed by Mann Whitney test.

Supplementary Figures

Figure S1. Liver, brain and body weight and brain morphology in *Csf1rko* and WT rats.

(A) Liver/body and (B) brain/body weight ratio in 3 wk-old male and female WT and *Csf1rko* rats. (C) Time course of body weight gain of male and female WT and *Csf1rko* rats.

(D) Representative images of WT (top panel) and *Csf1rko* (bottom panel) whole rat brain cut in the midsagittal plane. (E) Olfactory bulb, ventricular and cerebellar development of WT (top panel) and *Csf1rko* (bottom panel). (F) NeuN staining of sagittal slices from WT (top panel) and *Csf1rko* (bottom panel) brains including the cerebellum indicating neuronal distribution.

Figure S2. Histological analysis of *Csf1rko* and WT kidney, lung and intestine.

(A, B) Representative images of H&E staining in the kidney of (A) WT and (B) *Csf1rko* rats. Inner medulla (IM) outer stripe of the outer medulla (OSOM) and inner stripe of the outer medulla (ISOM) are enlarged. (C-F) Quantitative morphometry of villus architecture of WT and *Csf1rko* rats performed at 3 wks of age as described in Materials and Methods. (G) Representative images of elastin staining in the lung of WT and *Csf1rko* rats. (H) quantitative analysis of elastin stained area (% of area) of the lung of WT and *Csf1rko* rats. (I) Flow cytometry gating strategy to identify granulocytes in disaggregated lung. (J) Quantitation of granulocytes in 9 wk-old WT and *Csf1rko* rat lungs. p value based upon Mann Whitney test.

Figure S3. Comparison of mammary gland development in WT and *Csf1rko* rats.

(A) Representative mammary gland wholemounts from 9.5-week-old WT and *Csf1rko* rats. (B) Ductal growth relative to growth of the mammary fat pad. * $P < 0.05$, Student's t-test. (C) Photographs of rat mammary tissue in situ from WT and *Csf1rko* rats immediately post-euthanasia (black arrows). (D) IBA1 immunostaining of rat mammary tissue. E-cadherin (e-Cad) stains cells of the luminal lineage and cytokeratin 5 (Krt5) stains the basal lineage. Nuclei are stained with DAPI. White arrowheads point to intraepithelial $IBA1^+$ macrophages; white arrows point to $IBA1^+$ stromal

macrophages; asterisks show regions in *Csf1rko* tissue with poor basal cell development. Representative of n = 3 rats from each group.

Supplementary Table

Table S1. Comparative analysis of gene expression in the liver of WT and *Csf1rko* rats

A. Primary output of Kallisto quantitation of gene expression for livers from 3 male and 3 female WT and *Csf1ro* rats at 3 wks. List is ranked based upon ratio of expression KO/WT.

B. Analysis of differentially expressed genes (DEG) distinguishing WT and *Csf1rko* livers.

C. Co-expressed gene clusters generated from Biolayout analysis.

D. GO term enrichment for genes within the larger clusters of co-expressed genes.

Fig 1

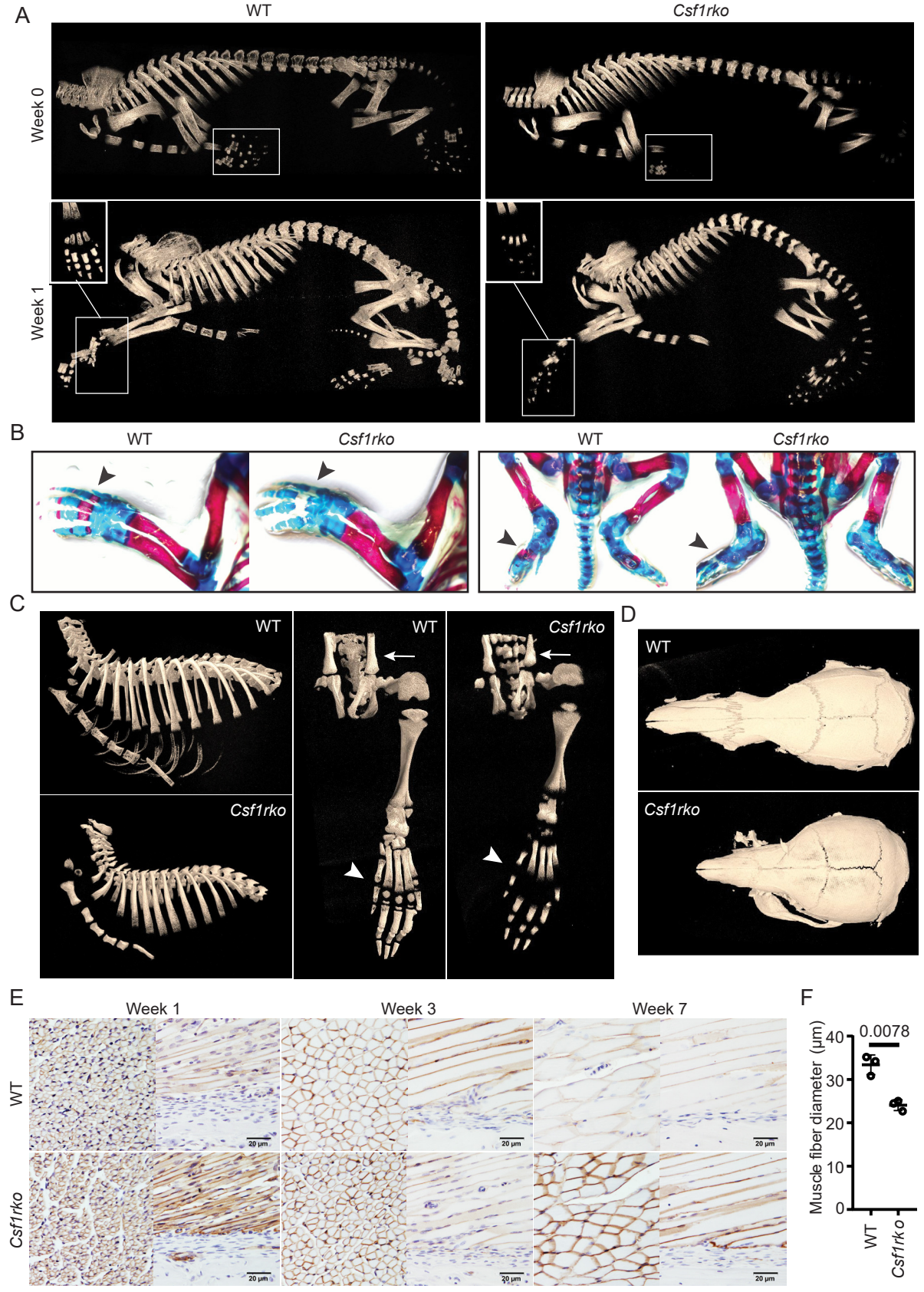
A
WT
Csf1rko
Week 0
Week 1
B
WT
Csf1rko
WT
Csf1rko
C
WT
Csf1rko
WT
Csf1rko
D
WT
Csf1rko
E
Week 1
Week 3
Week 7
WT
Csf1rko
20 µm
F
Muscle fiber diameter (µm)
0.0078
40
30
20
10
0
WT
Csf1rko

Fig 2

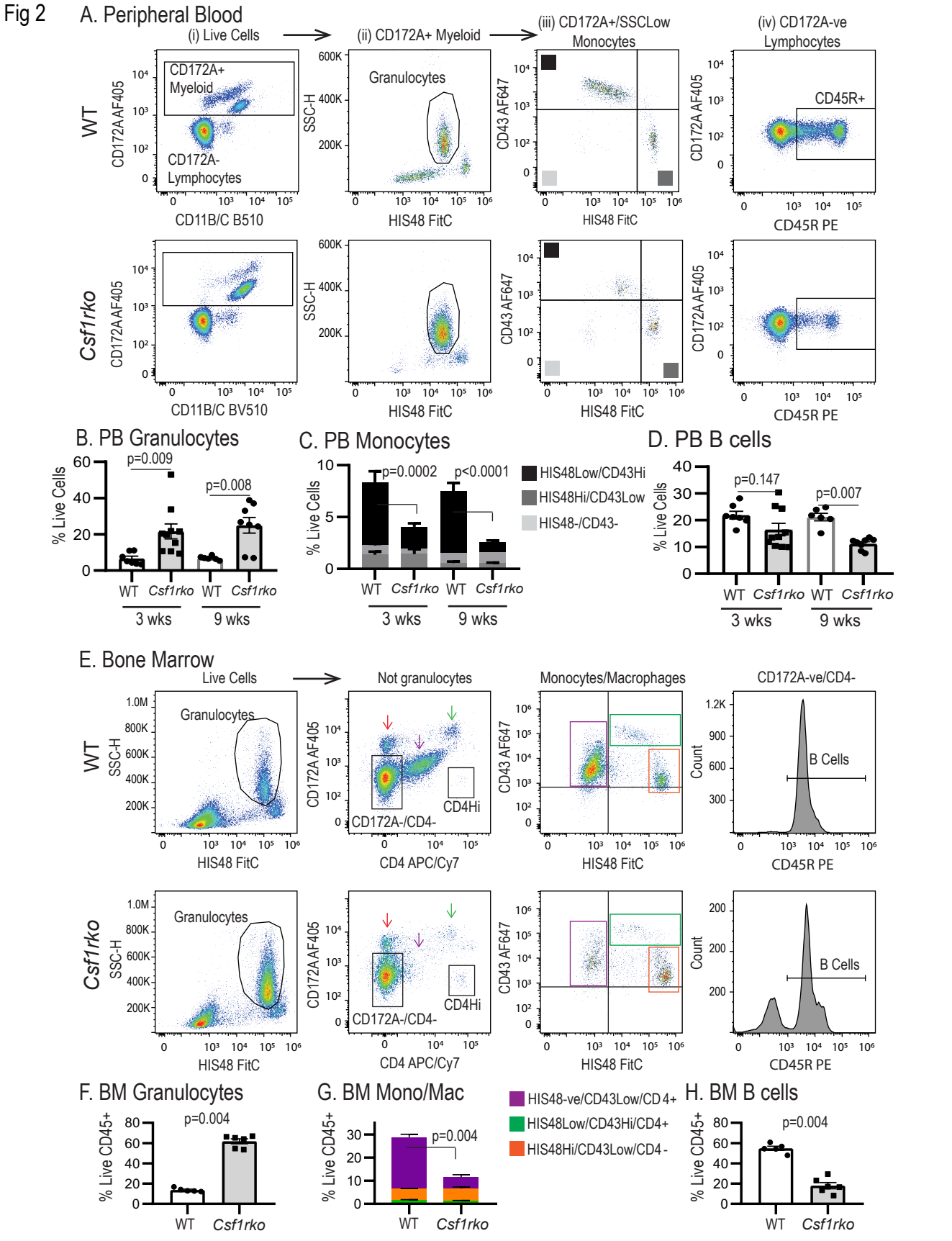
A. Peripheral Blood
(i) Live Cells
(ii) CD172A+ Myeloid
(iii) CD172A+/SSCLow Monocytes
(iv) CD172A-ve Lymphocytes
WT
Csf1rko
CD172A+ Myeloid
CD172A- Lymphocytes
CD172A AF405
CD11B/C B510
CD11B/C BV510
Granulocytes
SSC-H
HIS48 FitC
CD43 AF647
CD45R+
CD45R PE
B. PB Granulocytes
% Live Cells
p=0.009
p=0.008
WT
Csf1rko
3 wks
9 wks
C. PB Monocytes
p=0.0002
p<0.0001
HIS48Low/CD43Hi
HIS48Hi/CD43Low
HIS48-/CD43-
D. PB B cells
p=0.147
p=0.007
E. Bone Marrow
Live Cells
Not granulocytes
Monocytes/Macrophages
CD172A-ve/CD4-
CD172A-/CD4-
CD4Hi
CD4 APC/Cy7
Count
B Cells
F. BM Granulocytes
% Live CD45+
p=0.004
G. BM Mono/Mac
HIS48-ve/CD43Low/CD4+
HIS48Low/CD43Hi/CD4+
HIS48Hi/CD43Low/CD4-
H. BM B cells

Fig 3

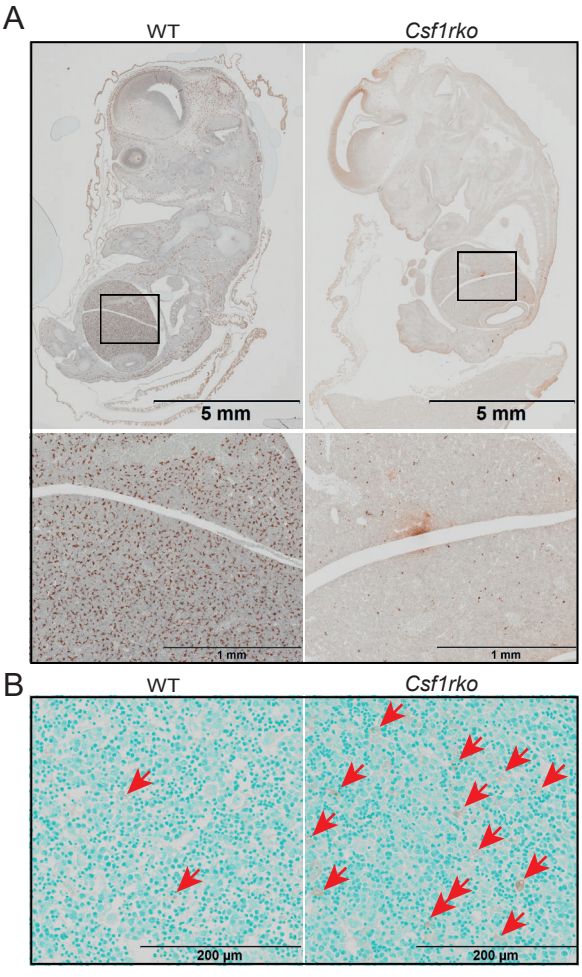

Fig 4

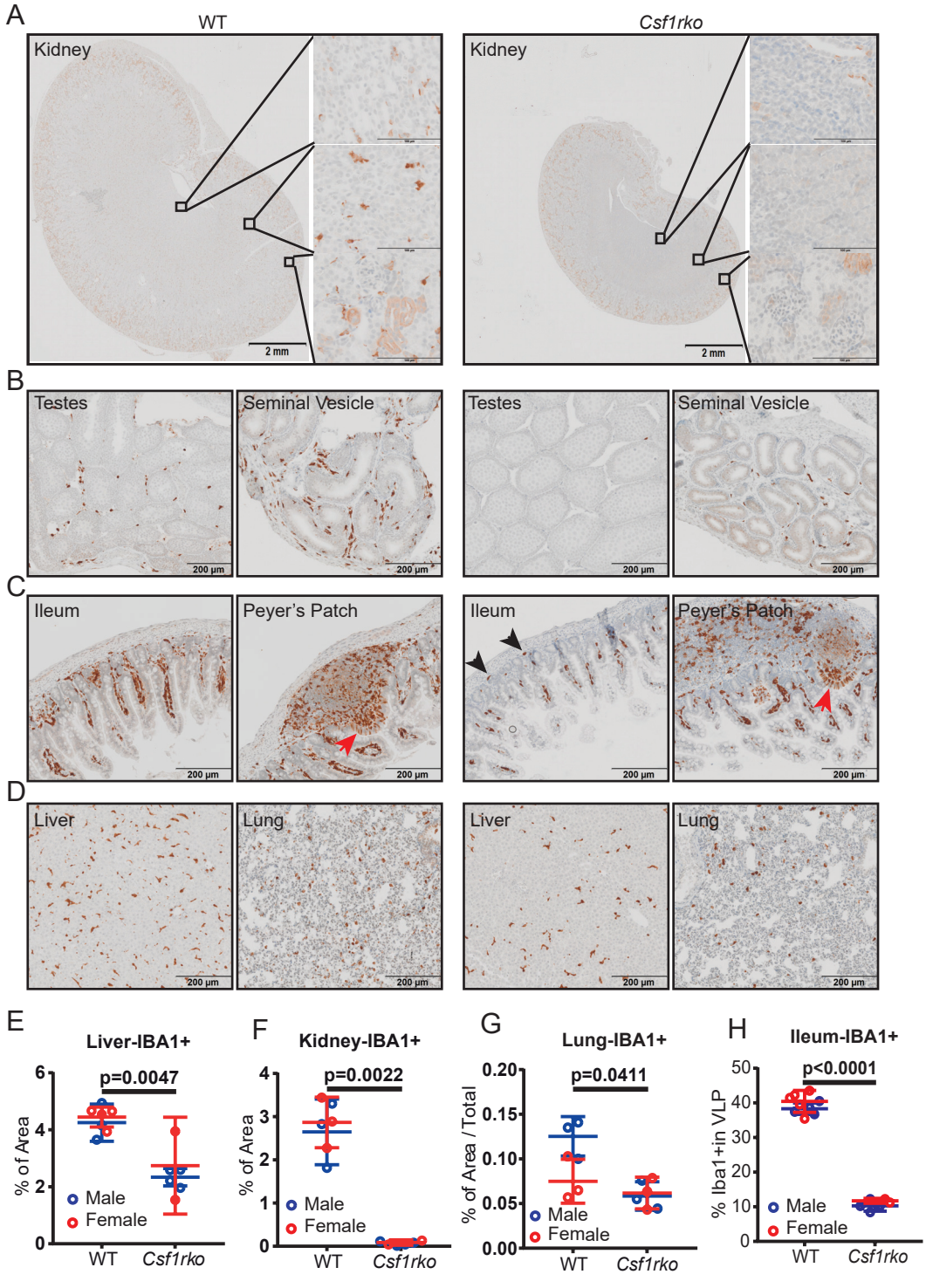
A
WT
Csf1rko
Kidney
Kidney
2 mm
2 mm
B
Testes
Seminal Vesicle
Testes
Seminal Vesicle
200 µm
C
Ileum
Peyer's Patch
Ileum
Peyer's Patch
D
Liver
Lung
Liver
Lung
E
Liver-IBA1+
p=0.0047
% of Area
Male
Female
WT
Csf1rko
F
Kidney-IBA1+
p=0.0022
% of Area
G
Lung-IBA1+
p=0.0411
% of Area / Total
H
Ileum-IBA1+
p<0.0001
% Iba1+in VLP

Fig 5

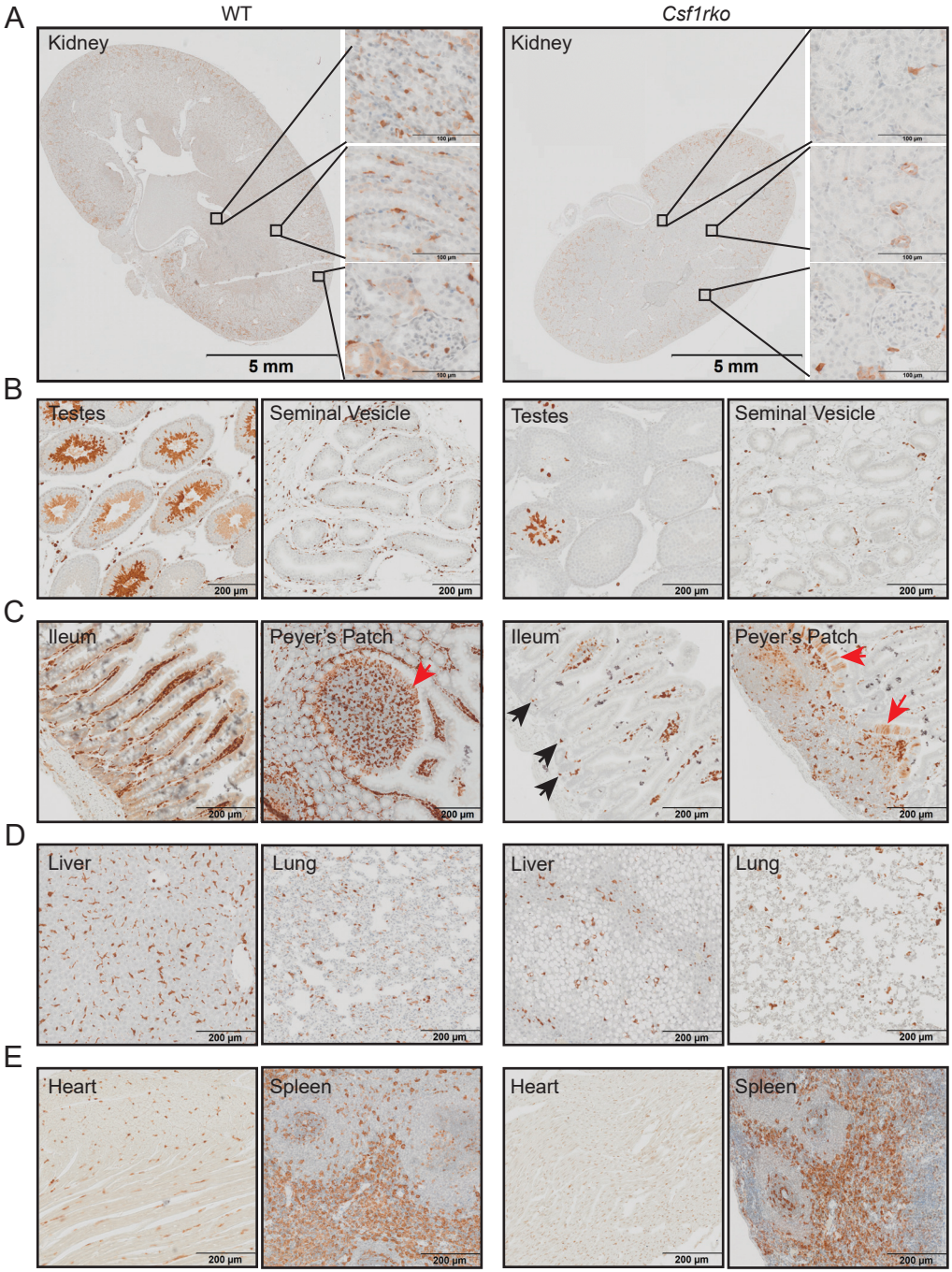
A
WT
Csf1rko
Kidney
Kidney
5 mm
5 mm
B
Testes
Seminal Vesicle
Testes
Seminal Vesicle
C
Ileum
Peyer's Patch
Ileum
Peyer's Patch
D
Liver
Lung
Liver
Lung
E
Heart
Spleen
Heart
Spleen
200 µm

Fig 6

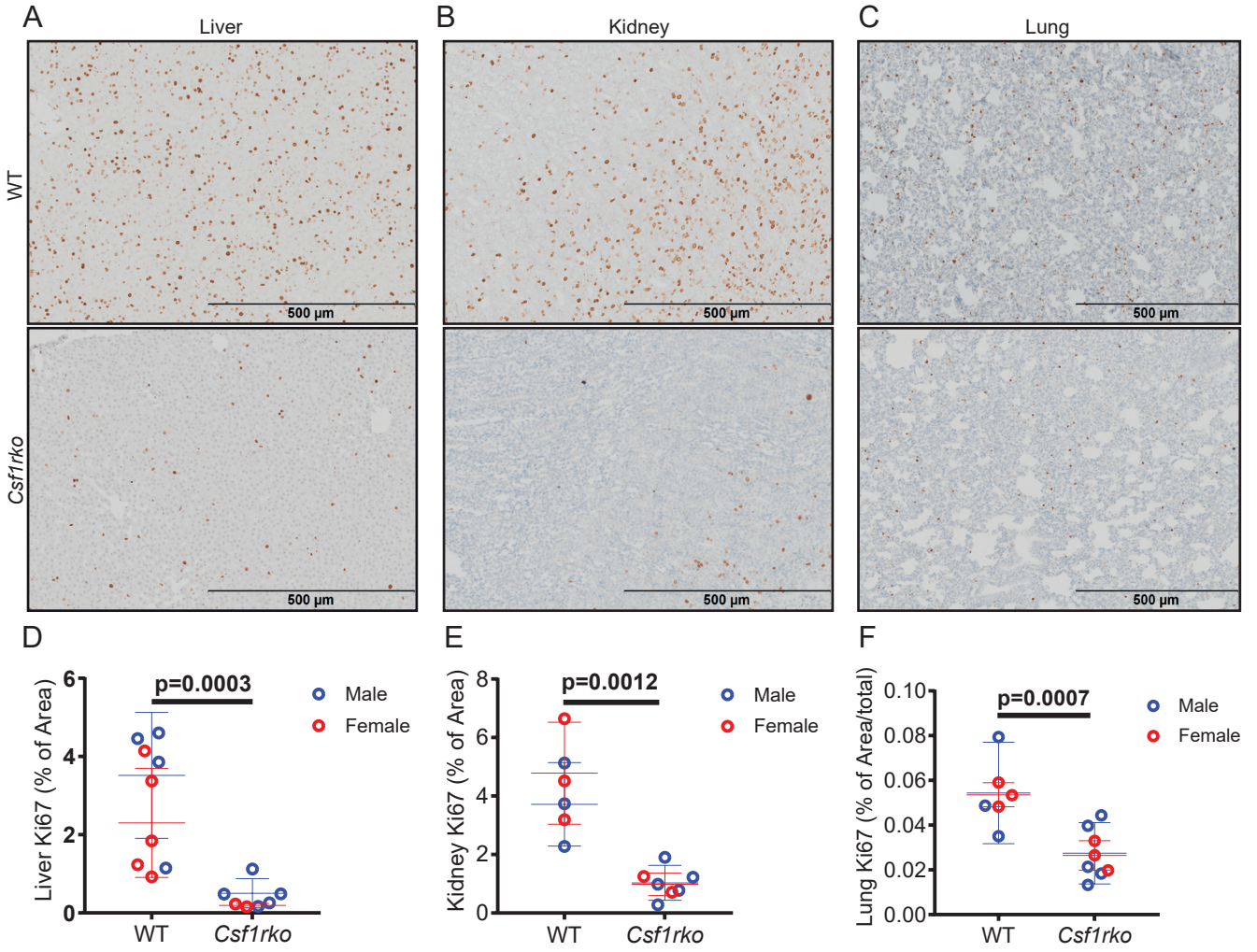
A
Liver
B
Kidney
C
Lung
WT
Csf1rko
500 µm
D
E
F
p=0.0003
p=0.0012
p=0.0007
Male
Female
Liver Ki67 (% of Area)
Kidney Ki67 (% of Area)
Lung Ki67 (% of Area/total)
WT
Csf1rko

Fig 7

A

Growth	Kupffer cells	Cell cycle	Lipid metabolism	Liver function
Angptl2, Angptl4, Ghr, Icoslg, Igfals, Igf1, Il34, Inhba, Inhbe, Ntf3, Igfbp1/2/5 Fst	Adgre1, Aif1, Axl, C1q, Ccl6, Cd163,Cd4, Cd5l, Cd68, Clec4f, Csf1r, Fcgr1a, Fcna, Hgpds, Ikzf4, Ly86, Mnda, P2rx7, Pld4, Ptger3, Ptgs1, Siglec1, Spi1, Timd2, Timd4, Vsig4	Birc5, Bub1, Ccna2, Cdk1, Cenpe, Foxm1, Fanca, Mcm5, Mki67,Pclaf, Pcna, Prc1, Pole2, Tcf19	Abcg3, Scly, Acsl3, Apoa4,Apoc2,Cyp5l Dgat2, Fasn, Fads1, Fabp1, Hes6, Hmgcs1, Ldlr, Lipc, Lrp1, Lss, Pvmk, Sc5d, Thrsp Wsp,	Adh7, Ahsg, Alb, Afm, Amy1a, Avpr1a, Ca3, C8a,Ces1c, Cfp, Crp, Ddc, Dio1, Cyp2b2, Hrg, Mbl1, Rbp2, Slc13a4, Slc16a11, Serpina3c, Serpina6

B

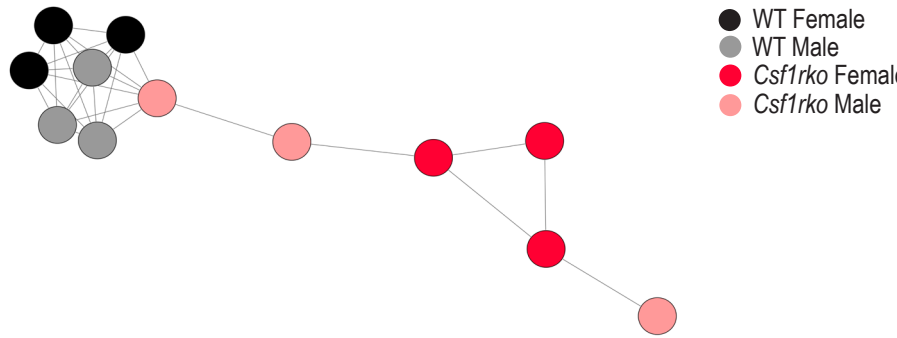

C

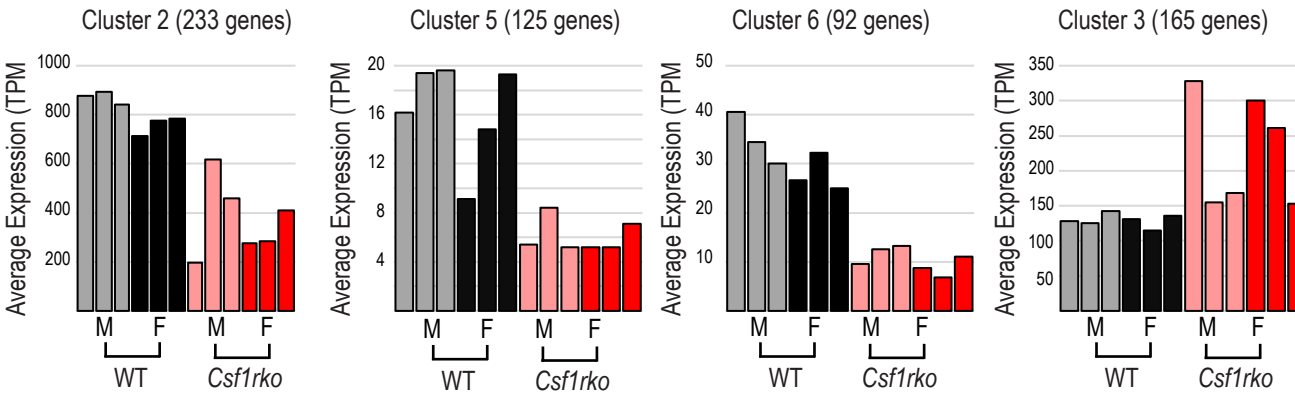

Fig 8

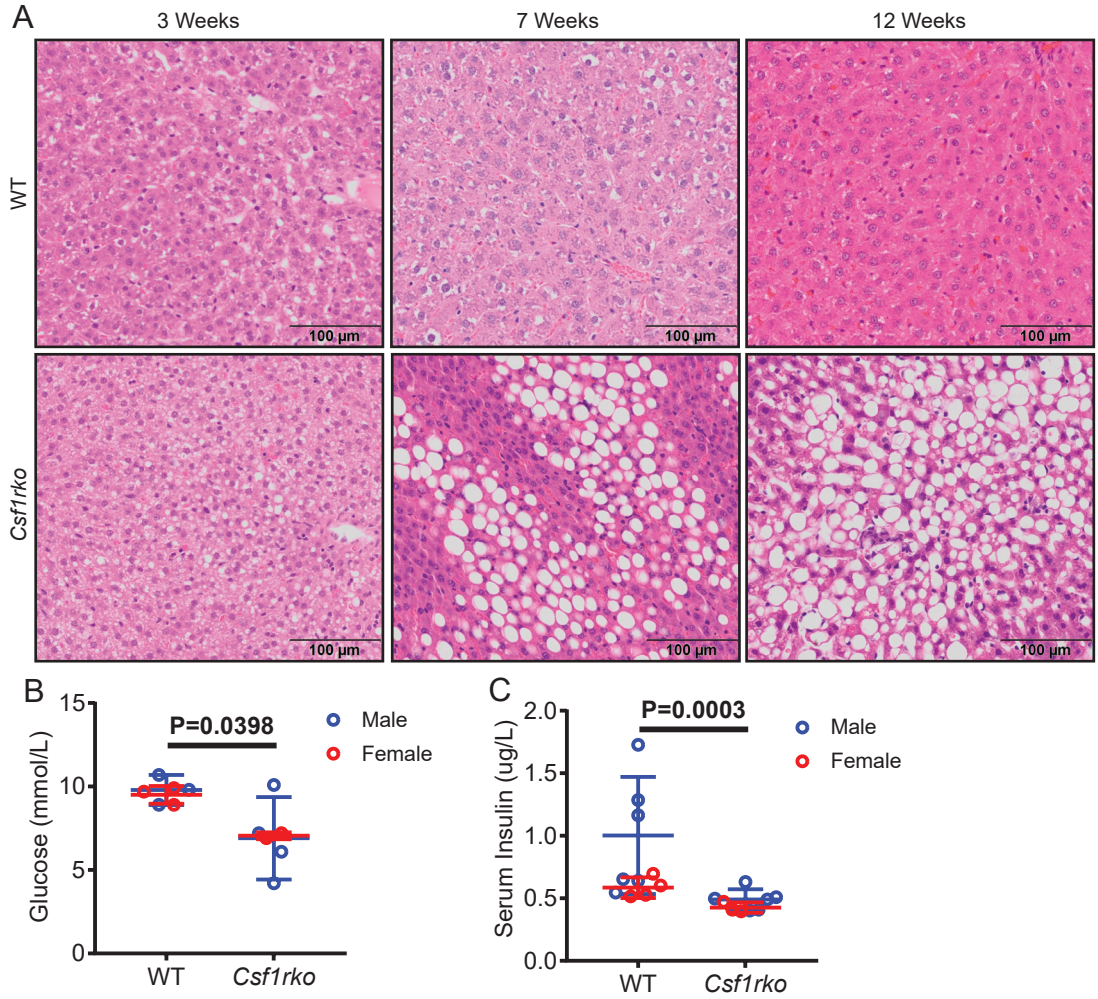
A
3 Weeks
7 Weeks
12 Weeks
WT
Csf1rko
100 µm
B
P=0.0398
Male
Female
Glucose (mmol/L)
15
10
5
0
WT
Csf1rko
C
P=0.0003
Male
Female
Serum Insulin (ug/L)
2.0
1.5
1.0
0.5
0.0
WT
Csf1rko

Fig 9

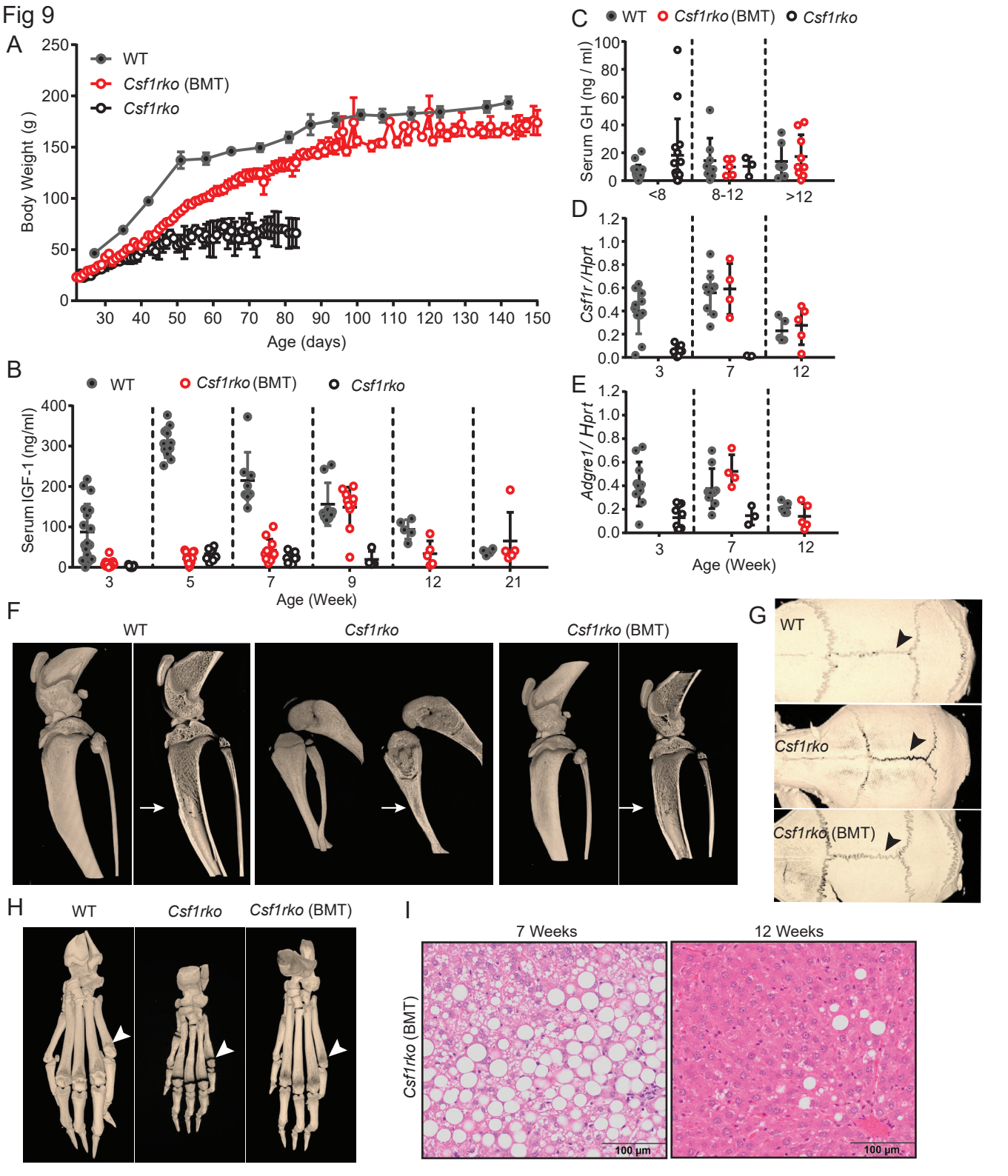
A
WT
Csf1rko (BMT)
Csf1rko
Body Weight (g)
Age (days)
B
WT
Csf1rko (BMT)
Csf1rko
Serum IGF-1 (ng/ml)
Age (Week)
C
WT
Csf1rko (BMT)
Csf1rko
Serum GH (ng / ml)
<8
8-12
>12
D
Csf1r / Hprt
3
7
12
E
Adgre1 / Hprt
3
7
12
Age (Week)
F
WT
Csf1rko
Csf1rko (BMT)
G
WT
Csf1rko
Csf1rko (BMT)
H
WT
Csf1rko
Csf1rko (BMT)
I
7 Weeks
12 Weeks
Csf1rko (BMT)
100 µm
100 µm

Fig 10

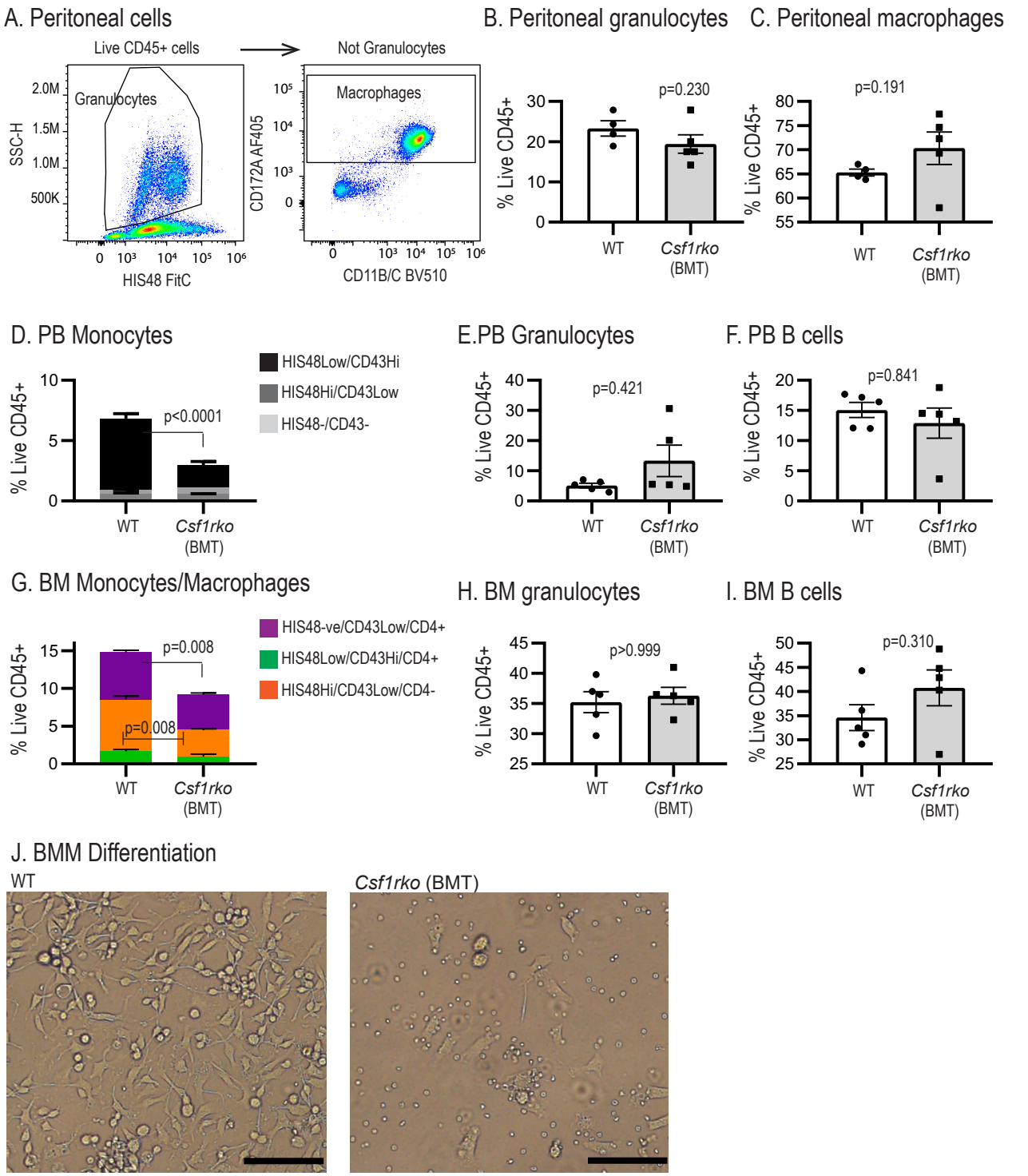
A. Peritoneal cells
Live CD45+ cells
Granulocytes
SSC-H
2.0M
1.5M
1.0M
500K
HIS48 FitC
Not Granulocytes
Macrophages
CD172A AF405
CD11B/C BV510
B. Peritoneal granulocytes
% Live CD45+
p=0.230
WT
Csf1rko (BMT)
C. Peritoneal macrophages
p=0.191
D. PB Monocytes
HIS48Low/CD43Hi
HIS48Hi/CD43Low
HIS48-/CD43-
p<0.0001
E.PB Granulocytes
p=0.421
F. PB B cells
p=0.841
G. BM Monocytes/Macrophages
HIS48-ve/CD43Low/CD4+
HIS48Low/CD43Hi/CD4+
HIS48Hi/CD43Low/CD4-
p=0.008
p=0.008
H. BM granulocytes
p>0.999
I. BM B cells
p=0.310
J. BMM Differentiation
WT
Csf1rko (BMT)

Fig S1

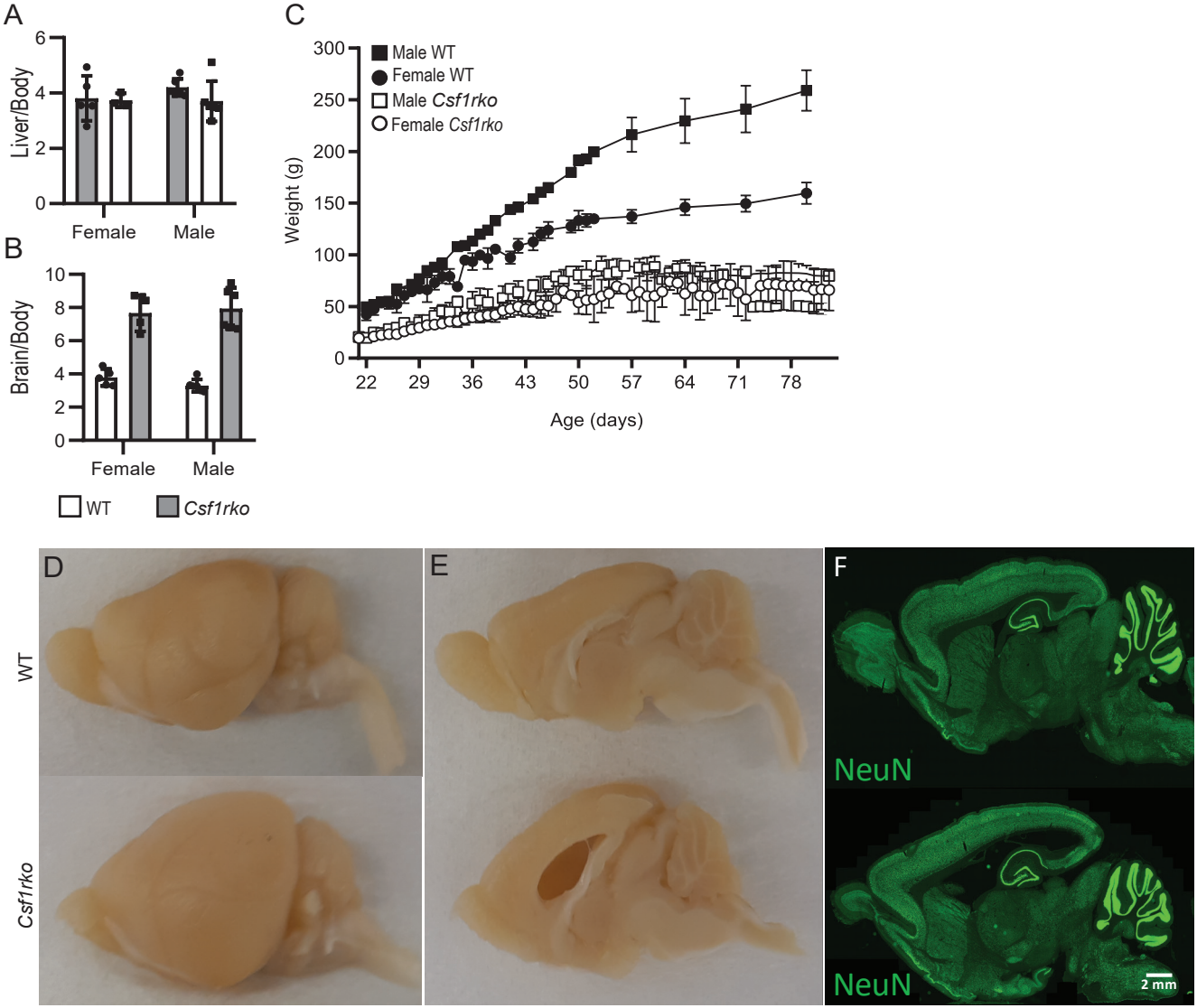
A
Liver/Body
6
4
2
0
Female
Male
B
Brain/Body
10
8
6
4
2
0
Female
Male
WT
Csf1rko
C
Male WT
Female WT
Male Csf1rko
Female Csf1rko
Weight (g)
300
250
200
150
100
50
0
22
29
36
43
50
57
64
71
78
Age (days)
D
E
F
WT
Csf1rko
NeuN
NeuN
2 mm

Fig S2

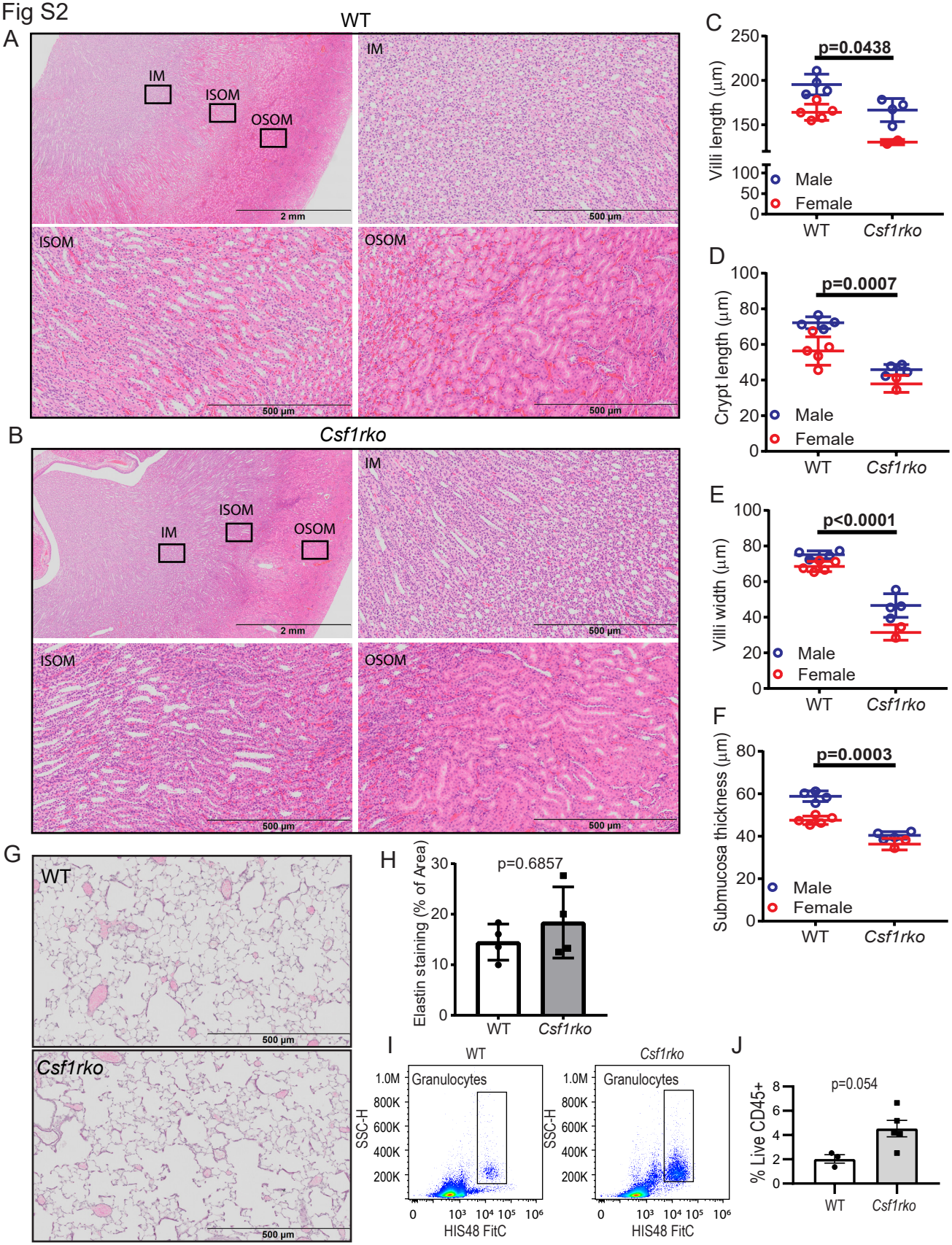
A
WT
IM
ISOM
OSOM
2 mm
500 µm
B
Csf1rko
C
p=0.0438
Villi length (µm)
Male
Female
WT
Csf1rko
D
p=0.0007
Crypt length (µm)
E
p<0.0001
Villi width (µm)
F
p=0.0003
Submucosa thickness (µm)
G
H
p=0.6857
Elastin staining (% of Area)
I
Granulocytes
SSC-H
HIS48 FitC
J
p=0.054
% Live CD45+

Fig S3

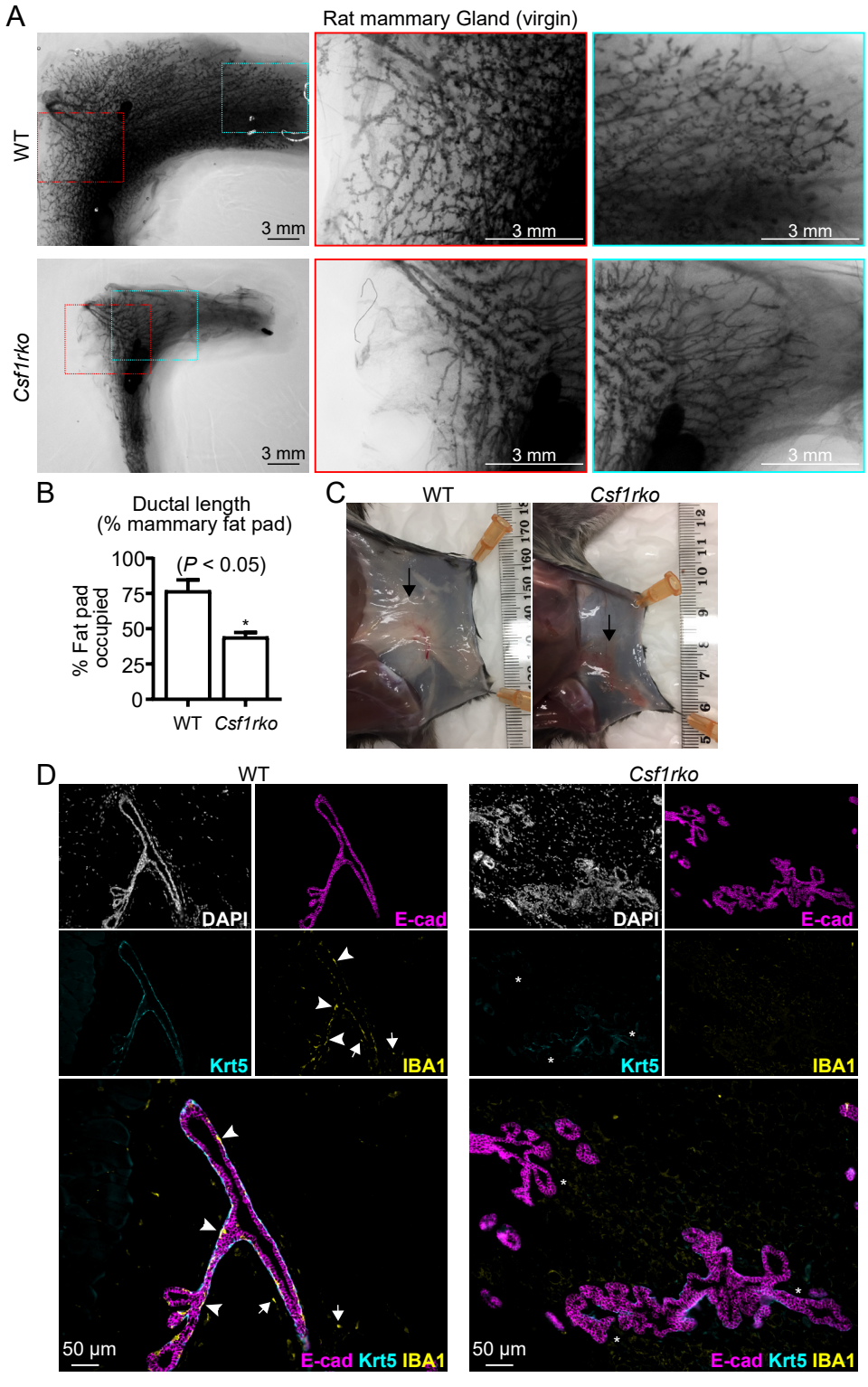
A
Rat mammary Gland (virgin)
WT
Csf1rko
3 mm
B
Ductal length
(% mammary fat pad)
(P < 0.05)
% Fat pad occupied
100
75
50
25
0
WT
Csf1rko
C
WT
Csf1rko
D
WT
Csf1rko
DAPI
E-cad
Krt5
IBA1
50 µm
E-cad Krt5 IBA1